

AD _____

Award Number: W81XWH-04-1-0323

TITLE: Task-Specific Optimization of Mammographic Systems

PRINCIPAL INVESTIGATOR: Robert Saunders

CONTRACTING ORGANIZATION: Duke University
Durham, North Carolina 27710

REPORT DATE: March 2005

TYPE OF REPORT: Annual Summary

PREPARED FOR: U.S. Army Medical Research and Materiel Command
Fort Detrick, Maryland 21702-5012

DISTRIBUTION STATEMENT: Approved for Public Release;
Distribution Unlimited

The views, opinions and/or findings contained in this report are those of the author(s) and should not be construed as an official Department of the Army position, policy or decision unless so designated by other documentation.

20050712 018

REPORT DOCUMENTATION PAGEForm Approved
OMB No. 074-0188

Public reporting burden for this collection of information is estimated to average 1 hour per response, including the time for reviewing instructions, searching existing data sources, gathering and maintaining the data needed, and completing and reviewing this collection of information. Send comments regarding this burden estimate or any other aspect of this collection of information, including suggestions for reducing this burden to Washington Headquarters Services, Directorate for Information Operations and Reports, 1215 Jefferson Davis Highway, Suite 1204, Arlington, VA 22202-4302, and to the Office of Management and Budget, Paperwork Reduction Project (0704-0188), Washington, DC 20503

| | | | | |
|---|---|--|--|--|
| 1. AGENCY USE ONLY (Leave blank) | | 2. REPORT DATE March 2005 | 3. REPORT TYPE AND DATES COVERED Annual Summary (15 Feb 04 -14 Feb 05) | |
| 4. TITLE AND SUBTITLE Task-Specific Optimization of Mammographic Systems | | | 5. FUNDING NUMBERS W81XWH-04-1-0323 | |
| 6. AUTHOR(S) Robert Saunders | | | | |
| 7. PERFORMING ORGANIZATION NAME(S) AND ADDRESS(ES) Duke University Durham, North Carolina 27710 E-Mail: rss@duke.edu | | | 8. PERFORMING ORGANIZATION REPORT NUMBER | |
| 9. SPONSORING / MONITORING AGENCY NAME(S) AND ADDRESS(ES) U.S. Army Medical Research and Materiel Command Fort Detrick, Maryland 21702-5012 | | | 10. SPONSORING / MONITORING AGENCY REPORT NUMBER | |
| 11. SUPPLEMENTARY NOTES | | | | |
| 12a. DISTRIBUTION / AVAILABILITY STATEMENT Approved for Public Release; Distribution Unlimited | | | 12b. DISTRIBUTION CODE | |
| 13. ABSTRACT (Maximum 200 Words) During this past year, our research has focused on four objectives. The first objective was to develop a simulation model for the radiographic appearance of breast masses and calcifications. This model was verified by a human observer performance experiment. The next objective explored the physical properties of a digital mammographic system, including resolution, noise, efficiency, and lag. The system was characterized for new beam qualities that used a tungsten anode, as these beams appear to produce higher quality digital images than conventional molybdenum beams. The third objective included physical measurements of display characteristics. This study introduced new means of removing the structured noise from Liquid Crystal Display (LCD) and Cathode Ray Tube (CRT) devices. The results from this study were applied to the fourth objective, which examined the impact of display resolution on the detection of breast masses and calcifications. We used two different observer models to inspect these images, including JNDMetrix, a visual discrimination model, and a non-prewhitening matched filter model with an eye filter. The results from this study will be used to guide human observer studies. Future work will explore the impact of dose reduction, detector properties, and image processing on detection of masses and calcifications. | | | | |
| 14. SUBJECT TERMS X-ray Imaging, Digital Imaging | | | 15. NUMBER OF PAGES 51 | |
| | | | 16. PRICE CODE | |
| 17. SECURITY CLASSIFICATION OF REPORT Unclassified | 18. SECURITY CLASSIFICATION OF THIS PAGE Unclassified | 19. SECURITY CLASSIFICATION OF ABSTRACT Unclassified | 20. LIMITATION OF ABSTRACT Unlimited | |

Table of Contents

| | |
|--|-----------|
| Cover..... | 1 |
| SF 298..... | 2 |
| Introduction..... | 4 |
| Body..... | 4 |
| Key Research Accomplishments..... | 7 |
| Reportable Outcomes..... | 8 |
| Conclusions..... | 9 |
| References..... | 10 |
| Appendices..... | 11 |

Introduction

X-ray mammography currently serves as the primary screening method for breast cancer. This research seeks to improve the efficacy of mammography by optimizing the entire imaging chain for the detection of breast masses and calcifications. Our research can be decomposed into two distinct areas. The first area involves a thorough understanding of the physical characteristics of the imaging chain. This includes experimental measurements of the resolution and noise of x-ray detectors and display devices. In addition, this requires modeling of physical processes, such as scatter, that impact image quality. The second area applies this physical data to simulation studies, allowing one to explore a variety of parameters in the imaging chain. Finally, the simulation procedures create images that simulate the resolution and noise of various imaging configurations. A combination of observer models and human observers view these simulated images in order to discover the impact of these resolution and noise settings on the detection of breast masses and calcifications.

Body

This section reviews the progress of the research in addressing the approved statement of work. We have included only those parts of the statement of work addressed by our work over the past year. Sections not included in this report are part of our future work.

Task 1: Create a simulation procedure for the anatomical background of mammographic images

- 1.1 *Acquire normal mammograms obtained on digital systems for analysis*
Working with colleagues from Emory University, we obtained 984 images acquired on an indirect flat-panel detector.
- 1.2 *Categorize the images into the four types of breast composition, as identified by the BIRADS system.*
- 1.3 *Analyze the geometrical features of these breasts and characterize them with a fixed number of scalar parameters, such as size.*
These two steps were included as they would aid in the creation on a routine to simulate mammographic backgrounds. As part of the research for anatomical simulation, we searched the literature for previous research on mammographic background simulation. We discovered and implemented the methods of Bochud, *et al* to emulate mammographic backgrounds by creating clustered lumpy backgrounds.¹ These simulated backgrounds appeared similar to real mammographic backgrounds, but did not capture all of the complexity of real anatomy. Therefore, we decided to use the mammographic data set obtained in 1.1 for our subsequent simulation experiments.
- 1.4 *Obtain mammograms from the Digital Database for Screening Mammography (DDSM) to analyze lesion characteristics*
We selected images from the DDSM that contained oval circumscribed, oval obscured, irregular ill-defined, and irregular spiculated masses. In addition, we selected images that contained fine linear branching and pleomorphic calcifications. We segmented these mammograms into regions of 2.56 cm x 2.56 cm centered on the mass or calcification.
- 1.5 *Analyze the features of specific lesion types*
We analyzed the images obtained from the DDSM to create a model of the radiographic appearance of breast lesions. This model was described in our 2004 IWDM proceedings article in Appendix III.
- 1.6 *Create a program that can create images with breast anatomy and breast lesions that allows for user input of specific scalar parameters, such as size.*
We created a program that allowed one to insert simulated masses and calcifications into normal anatomical backgrounds. The details of this program were disclosed in our 2004 IWDM proceedings article in Appendix III. In addition, this program served a crucial role in our recent research on the impact of display image quality, as disclosed in Appendix II.

As noted in 1.2 and 1.3, the simulated mammographic backgrounds lacked the complexity of real backgrounds. We therefore used actual digital mammograms for our simulation experiments.

1.7 *Establish mapping technique to determine grayscale values of image using sigmoid curve transformation.*

To conduct this task, an experienced mammographer reviewed the digital images obtained in 1.1 and window and leveled each mammogram to produce a clinically relevant appearance. We recorded the parameters for each image and fit a sigmoid curve to each window and level function. We then applied the appropriate transformation to each image in order to simulate the correct clinical appearance. This stage was disclosed in our 2005 SPIE proceedings article in Appendix II.

Task 3: Create an empirical model that relates the resolution and noise of a digital mammographic system to the detectability of breast lesions.

3.1 *Compile a list of MTFs and NPS for commercial radiographic systems, including image processing algorithms and displays.*

We have begun compiling a list of MTFs and NPSs for several mammographic systems. In addition, we have conducted some studies to directly measure the physical characteristics of mammographic systems. Please refer to Appendix I for one study where we measured the performance of a clinical prototype digital mammographic system.

Task 5: Utilize the empirical model to examine the effect of dose on the detection of microcalcifications and masses and determine the minimum allowable dose level for "safe" mammographic imaging.

5.1 *Determine the relationship between dose and noise amplitude for the three specific digital mammographic systems through published measurements.*

We determined the magnitude of the signal to noise ratio for a given dose by the equation:

$$SNR_{Actual}^2 = DQE(0) \cdot SNR_{Ideal}^2 \quad (1)$$

where SNR_{Ideal} was computed using a program by Boone to generate x-ray spectra² and $DQE(0)$ was determined from published measurements. This signal to noise ratio was mapped to a graylevel variance using the exposure-pixel value relationship for the detector.

5.2 *Determine the effect of scatter utilizing previously published models.*

We determined the magnitude of scatter by using previously published data by Boone.³ Our group measured the magnitude of scatter reduction accomplished by the antiscatter grid. The scatter to primary ratios were then discounted by the scatter reduction from the grid. The effect of scatter was incorporated by reducing the contrast of our simulated lesions by the magnitude of the scattered radiation.

5.3 *Using the previously developed empirical model to analyze the effect of dose on the detectability of masses and microcalcifications.*

We have generated four image sets using the mammographic data obtained in 1.1. The first set was obtained at full dose and the next three sets have added noise to simulate half, quarter, and eighth dose, respectively. Two different observer models analyzed these image sets, a visual discrimination model and a non-prewhitening matched filter with eye filter model. We are currently examining the results from these observer models.

Task 6: Apply the empirical model to ascertain the effect of a specific image processing algorithm, unsharp masking, on lesion detection and optimize its utilization.

6.1 *Examine the clinical parameters used for unsharp masking.*

Several types of unsharp masking are used in clinical practice. We implemented the most basic type of multiscale processing, consisting of an unsharp masking stage and a contrast equalization stage. The form of this processing and parameters were determined from previously published methods.⁴

Task 7: Employ the model to examine the influence of two specific display characteristics, display magnification and display resolution, on lesion detection and thus develop guidelines for optimized viewing of digital mammograms.

7.2 *Determine the resolution and noise for four display devices, three common Cathode Ray Tube (CRT) devices and one Liquid Crystal Display (LCD) device.*

Using a high-quality CCD camera, we measured the resolution and noise of two CRT displays and three LCD devices. As LCDs are becoming increasingly common in clinical systems, we decided to include more of a focus on LCD displays than we proposed in the statement of work. We have written a manuscript describing our measurement protocol and experimental results and submitted it to Medical Physics in mid-March 2005.

- 7.3 *Fit the resolution and noise properties of the combined display and detector system using the generalized curve-fitting algorithm.*
After obtaining the resolution and noise characteristics, we fit each of them with a multi-parameter exponential function. This provided us with a functional form for the resolution and noise data.
- 7.4 *Input the above into the empirical model in order to develop guidelines for optimized display of mammographic images.*
Instead of an empirical model, we used observer models to examine the impact of different display resolutions on the detection of masses and calcifications. Please refer to our 2005 SPIE proceedings article in Appendix II for the full details of this project.

Key Research Accomplishments

- Acquired a large data set of normal digital mammograms.
- Developed model for radiographic appearance of breast masses and calcifications and implemented lesion simulation program.
- Measured resolution and noise of five medical displays, representing both CRT and LCD devices.
- Created large image set with resolution properties emulating those of commercial medical displays.
- Created large image set that simulated the effects of reduced dose.
- Implemented observer model for examining image sets, based on a non-prewhitening matched filter model with eye filter.
- Measured physical characteristics of clinical prototype mammographic system.
- Researched image processing techniques and wrote program based on a common image processing algorithm.

Reportable Outcomes

CONFERENCE PRESENTATIONS

R.S. Saunders Jr., E. Samei, J. Johnson, and J. Baker, "Effect of Display Resolution on the Detection of Mammographic Lesions," SPIE Medical Imaging 2005: Image Perception, Observer Performance, and Technology Assessment (2005).

R. S. Saunders Jr., E. Samei, J. Baker, "Simulation of Mammographic Lesions," Radiological Society of North America Annual Meeting (2004).

R. S. Saunders Jr, A. Farshchi, E. Samei, "Measurement of Display Resolution for Commercial Medical Displays," Radiological Society of North America Annual Meeting (2004).

R. S. Saunders Jr., E. Samei, J. Y. Lo and J. L. Jesneck, "Physical Characterization of a Selenium-based Full Field Digital Mammography Detector," 7th International Workshop on Digital Mammography (2004).

R. S. Saunders Jr., E. Samei, and J. Baker, "Simulation of Breast Lesions," 7th International Workshop on Digital Mammography (2004).

REFEREED JOURNAL ARTICLES

R.S. Saunders Jr., E. Samei, J.L. Jesneck, and J.Y. Lo, "Physical characterization of a prototype selenium-based full field digital mammography detector," Med. Phys. **32**, 588-599 (2005).

Conclusions

This year, we have developed several tools that allow us to explore the impact of resolution and noise on the detection of mammographic lesions. First, we have developed a routine that inserts simulated masses or calcifications into a normal mammographic background. Second, we have measured the physical properties of a clinical mammographic detector and several medical display devices. Third, we have acquired a large data set of mammographic images. Applying these tools, we have explored two questions this year. The first question explored the impact of display resolution on the detection of breast masses and calcifications. The second question explored the effect of reduced dose on the detection of breast lesions. Both of these questions have immediate impact on clinical care, as they will determine which medical displays are appropriate for reading mammograms and whether women may be imaged using a lower dose. Future work will include examining the effect of image processing and the relative merit of different mammographic detectors on the detection of breast lesions.

References

- 1 F. O. Bochud, C. K. Abbey and M. P. Eckstein, "Statistical texture synthesis of mammographic images with clustered lumpy backgrounds," *Optics Express* **4**, (1999).
- 2 J. M. Boone, T. R. Fewell and R. J. Jennings, "Molybdenum, rhodium, and tungsten anode spectral models using interpolating polynomials with application to mammography," *Med Phys* **24**, 1863-1874 (1997).
- 3 J. M. Boone, K. K. Lindfors, V. N. Cooper, 3rd and J. A. Seibert, "Scatter/primary in mammography: comprehensive results," *Med Phys* **27**, 2408-2416 (2000).
- 4 M. Stahl, T. Aach and S. Dippel, "Digital radiography enhancement by nonlinear multiscale processing," *Med Phys* **27**, 56-65 (2000).

Appendices

Appendix I: *2005 Medical Physics article on physical characteristics of a digital mammographic system*
R.S. Saunders Jr., E. Samei, J.L. Jesneck, and J.Y. Lo, "Physical characterization of a prototype selenium-based full field digital mammography detector," *Med. Phys.* **32**, 588-599 (2005).

Appendix II: *2005 SPIE proceedings article on impact of display resolution on detection of breast lesions*
R.S. Saunders Jr., E. Samei, J. Johnson, and J. Baker, "Effect of Display Resolution on the Detection of Mammographic Lesions," *Proc. SPIE* **5749** (2005).

Appendix III: *2004 IWDM proceedings article on simulation of the radiographic appearance of breast lesions*
R. S. Saunders Jr., E. Samei, and J. Baker, "Simulation of Breast Lesions," *Proceedings of IWDM* (2004).

Appendix IV: *2004 IWDM proceedings article on physical characteristics of a digital mammographic system*
R. S. Saunders Jr., E. Samei, J. Y. Lo and J. L. Jesneck, "Physical Characterization of a Selenium-based Full Field Digital Mammography Detector," *Proceedings of IWDM* (2004).

Physical characterization of a prototype selenium-based full field digital mammography detector

Robert S. Saunders, Jr.

Duke Advanced Imaging Laboratories

Departments of Physics and Radiology, Duke University, Durham, North Carolina 27710

Ehsan Samei

Duke Advanced Imaging Laboratories

Departments of Radiology, Physics, and Biomedical Engineering, Duke University, Durham, North Carolina 27710

Jonathan L. Jesneck

Duke Advanced Imaging Laboratories

Departments of Biomedical Engineering and Radiology, Duke University, Durham, North Carolina 27710

Joseph Y. Lo

Duke Advanced Imaging Laboratories

Departments of Radiology and Biomedical Engineering, Duke University, Durham, North Carolina 27710

(Received 23 July 2004; revised 15 November 2004; accepted for publication 14 December 2004; published 3 February 2005)

The purpose of this study was to measure experimentally the physical performance of a prototype mammographic imager based on a direct detection, flat-panel array design employing an amorphous selenium converter with 70 μm pixels. The system was characterized for two different anode types, a molybdenum target with molybdenum filtration (Mo/Mo) and a tungsten target with rhodium filtration (W/Rh), at two different energies, 28 and 35 kVp, with approximately 2 mm added aluminum filtration. To measure the resolution, the presampled modulation transfer function (MTF) was measured using an edge method. The normalized noise power spectrum (NNPS) was measured by two-dimensional Fourier analysis of uniformly exposed mammograms. The detective quantum efficiencies (DQEs) were computed from the MTFs, the NNPSs, and theoretical ideal signal to noise ratios. The MTF was found to be close to its ideal limit and reached 0.2 at 11.8 mm^{-1} and 0.1 at 14.1 mm^{-1} for images acquired at an RQA-M2 technique (Mo/Mo anode, 28 kVp, 2 mm Al). Using a tungsten technique (MW2; W/Rh anode, 28 kVp, 2 mm Al), the MTF went to 0.2 at 11.2 mm^{-1} and to 0.1 at 13.3 mm^{-1} . The DQE reached a maximum value of 54% at 1.35 mm^{-1} for the RQA-M2 technique at 1.6 $\mu\text{C}/\text{kg}$ and achieved a peak value of 64% at 1.75 mm^{-1} for the tungsten technique (MW2) at 1.9 $\mu\text{C}/\text{kg}$. Nevertheless, the DQE showed strong exposure and frequency dependencies. The results indicated that the detector offered high MTFs and DQEs, but structured noise effects may require improved calibration before clinical implementation. © 2005 American Association of Physicists in Medicine. [DOI: 10.1118/1.1855033]

Key words: image quality, mammography, modulation transfer function, normalized noise power spectrum, detective quantum efficiency, digital imaging

I. INTRODUCTION

Breast cancer remains the second leading cause of cancer death for women in the United States. The American Cancer Society (ACS) estimates that in 2004, 215 990 new cases of invasive breast cancer will be diagnosed and 40 110 women will die from the disease in the United States.¹ Early detection of this disease holds the key for survival, as more treatment options exist for early stage cancers and treatments tend to be more successful at this stage. X-ray mammography continues to be widely regarded as the most effective early-detection screening tool available today.^{2,3} X-ray mammography places severe demands, however, on an imaging system. A system must capture small, low contrast anatomical details, as the early signs of cancer are often very subtle. While mammography has experienced notable advancements

in recent years, further improvement is required as up to 22% of cancers are missed at the initial screening.⁴

Full Field Digital Mammography (FFDM) offers the promise of improving mammographic image quality and therefore increasing the utility of this screening procedure.⁵⁻⁷ As images are stored in a digital format, a radiologist can view the images at any workstation or many clinicians can have simultaneous access to the images. The use of image processing algorithms enhances various features in the image. In addition, these systems have the potential to improve mammographic imaging by separating each stage of the imaging chain, from detection to image processing to display, allowing each step to be independently optimized.

The current state of the art in digital mammography is solid-state flat-panel detectors.⁸ Flat-panel detectors can be subdivided into two categories, direct and indirect, named

for the mechanisms used to detect x-rays.^{9,10} In direct detectors, a photoconductive layer absorbs an incoming x-ray photon and converts it to electric charge. A voltage applied across the photoconductor then draws the charges toward the pixel electrodes.^{11,12} In contrast, indirect detectors utilize a scintillation layer that converts the x-ray photon into visible light photons, which are subsequently absorbed by photosensitive elements.^{13,14} Because of the different physical mechanisms used to detect photons, the image quality characteristics of these detectors differ substantially. Several prior studies have substantiated some of these differences.^{9,10,15,16} In addition, two previous studies have examined limited aspects of image quality for selected mammographic detectors using amorphous selenium.^{17,18}

The main purpose of this work was to comprehensively evaluate the physical image quality characteristics of an early prototype mammographic detector based on a direct detection flat-panel array design that employed an amorphous selenium converter. Three key metrics of image quality were evaluated for several radiographic techniques, the modulation transfer function (MTF), normalized noise power spectrum (NNPS), and detective quantum efficiency (DQE), which described the resolution, noise, and signal to noise performance of the detector, respectively.^{19–24} As previous research has shown that selenium detectors can exhibit image lag and ghosting,²⁵ this research also examined the lag performance of the detector.

A secondary objective of this research was to consider new beam qualities for digital mammography. Traditionally, screen-film mammography was performed using a beam from a molybdenum target with molybdenum filtration.²⁶ This beam quality might not be optimal for digital mammography, however, given the different energy sensitivities and greater dynamic range of digital detectors. Several researchers had suggested that other beam qualities could allow for better image quality for digital mammography.^{17,27–30} Therefore, the study examined the image quality characteristics for two different anode types, a molybdenum target with molybdenum filtration and a tungsten target with rhodium filtration, and for two different energies, 28 kVp and 35 kVp, with added aluminum filtration.

II. METHODS AND MATERIALS

A. Detector description

The detector investigated in this study was an early prototype mammographic imager based on a direct detection flat-panel array design that employed an amorphous selenium converter (Mammomat Novation^{DR}; Siemens Medical Solutions; Erlangen, Germany). The detector utilized a 250 μm amorphous selenium photoconductive layer coupled to a matrix of pixels, each with a storage capacitor and amorphous silicon switching transistor.¹⁸ The active detector area was 23.3 cm \times 28.7 cm consisting of 3328 \times 4096 square pixels. Each pixel was placed with a 70 μm pixel pitch and offered a fill factor of greater than 90%. This product has since received FDA approval.

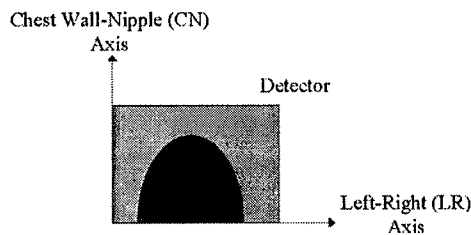


FIG. 1. Coordinate system for physical measurements. These axes are labeled by the anatomy imaged in the craniocaudal view.

Prior to evaluation, the standard antiscatter grid and compression paddle were removed from the system. For most measurements, the standard detector cover was placed on the system. For the MTF measurements, the detector cover was removed so that an edge device could be placed as close as possible to the active selenium layer to minimize focal spot blur.

The coordinate system used to describe the system, as shown in Fig. 1, referred to the anatomical features as viewed on a craniocaudal view. There were two main axes, the chest wall–nipple (CN) axis as well as the left–right (LR) axis. By examining the system performance along these two orthogonal axes, one was able to identify any asymmetries.

B. Image acquisition

A high-frequency, multiphase x-ray generator (Mammomat Novation^{DR}), for which the high voltage accuracy was verified to be within $\pm 5\%$, served as the x-ray source for the system. The anode was operated with a large focal spot of 0.3 mm (IEC), nominal, for all image acquisitions. No post-processing was applied to the images. All images were transferred to a research computer as 14-bit, raw data for analysis.

Prior to image acquisition, the detector underwent routine detector calibration to correct for dead pixels and gain non-uniformities. The process formed a dead pixel map by detecting inactive pixels in a flat-field image acquired at 28 kVp with a 4 cm PMMA slab in the beam. A gain map was similarly computed from the average of eight flat-field images also acquired at 28 kVp with a 4 cm PMMA slab in the beam. As no images in this research utilized an antiscatter grid, the calibration was performed without a grid in place. The system corrected all subsequently acquired images using the gain and dead pixel maps.

For all image acquisitions, the exposure to the detector was measured using a calibrated ionization chamber (1515 x-ray monitor with 10X5-6M dedicated mammography ionization chamber, Radcal Corporation, Monrovia, CA) placed at 48 cm from the focal spot. As reported in previous studies, this ionization chamber had little energy dependence over mammographic energies.³¹ Manufacturer specifications note that the calibration accuracy of the chamber was $\pm 4\%$ (at 20 kVp, 0.26 mm Al HVL) with $\pm 5\%$ energy dependence in the 10 keV to 40 keV range. The exposures incident on the detector, located at 65 cm distance from the focal spot, were estimated from the measured exposure values using the inverse-square law.

TABLE I. Beam qualities used for physical characterization of the detector. The aluminum used for the added filtration had $\geq 99\%$ purity.

| Name | Anode target | Anode filtration | kVp | Added filtration (mm Al) | Half-value layer (mm Al) |
|--------|--------------|--------------------------------|-----|--------------------------|--------------------------|
| RQA-M2 | Molybdenum | Molybdenum (30 μm) | 28 | 2 | 0.6 |
| RQA-M4 | Molybdenum | Molybdenum (30 μm) | 35 | 1.8 | 0.68 |
| MW2 | Tungsten | Rhodium (50 μm) | 28 | 2 | 0.79 |
| MW4 | Tungsten | Rhodium (50 μm) | 35 | 2 | 0.92 |

Four different beam qualities were utilized for the image quality measurements, as outlined in Table I. Two molybdenum techniques, RQA-M2 and RQA-M4, were chosen from the International Electrotechnical Commission (IEC) standard 61267-2.³² The standard specified the anode type, anode filtration, kVp, and half-value layer for each beam quality. Aluminum filtration was then placed in the beam to produce the desired half-value layer. The IEC standard did not include corresponding tungsten techniques for mammographic applications. To facilitate meaningful comparisons between detector systems, two additional tungsten techniques, MW2 and MW4, were used that had similar characteristics to those of the molybdenum techniques, RQA-M2 and RQA-M4. The half-value layers for these four beam qualities were measured using a narrow geometry and added aluminum filtration in 0.1 mm increments around the estimated half-value layer thickness. The half-value layer thicknesses were then estimated from logarithmic interpolation of the measured exposure values.³²

C. Linearity

Linearity was determined by exposing the detector to a wide range of uniform x-ray exposures for each of the four radiographic techniques described above. The average pixel values were computed from a 14.3 cm \times 14.3 cm region located near the chest wall section of the detector. From this, the relationships between mean pixel value and exposure were ascertained for each technique.

D. Modulation transfer function

An edge method, reported in previous publications,^{9,10,33-36} was used to measure the presampled MTF. A 0.1 mm Pt-Ir edge was placed in contact with the detector at 1 cm distance from the chest wall edge of the detector. The device was oriented at a 3°–6° angle with respect to the pixel array. Edge images were then acquired at each of the four radiographic techniques at relatively high exposure values of 16.2 $\mu\text{C}/\text{kg}$ (62.6 mR), 15.3 $\mu\text{C}/\text{kg}$ (59.2 mR), 9.52 $\mu\text{C}/\text{kg}$ (36.9 mR), and 9.75 $\mu\text{C}/\text{kg}$ (37.8 mR) for RQA-M2, RQA-M4, MW2, and MW4 techniques, respectively.

A previously reported routine³⁷ analyzed the edge images in a region around the edge (21.2 mm \times 35.8 mm) to deter-

mine the presampled modulation transfer function (MTF). In summary, first a double Radon transformation determined the angle of the edge transition with 0.01° accuracy. The edge spread function (ESF) was computed by projecting the image data along lines parallel to the edge transition using bin sizes of 0.1 pixels. To minimize noise, the ESF was smoothed using a modest fourth-order moving polynomial fit and differentiated to form the line spread function (LSF). A Hanning window with 10 mm width was then applied to the LSF to force the tails of the LSF to zero. Finally, the presampled MTF was computed as the normalized Fast Fourier Transform of the LSF.

E. Normalized noise power spectrum

To characterize the system noise, images were acquired of uniform beams of radiation for the different techniques, while the exposure was simultaneously measured with an ionization chamber. The NNPS was then computed from these flat-field images using previously published methods.³⁶⁻³⁸ A large region near the chest wall side of the detector, excluding the edges of the image, was used for analysis. This region was segmented into 256 sequential regions of interest (ROIs) of 128 \times 128 pixels. A two-dimensional polynomial surface was subtracted from each region of interest (ROI) to minimize background trending and a Hamming window was applied to each ROI so that the edges of the ROI went to zero. To account for intensity variations in the image, each ROI was then scaled by the ratio of its mean to the mean pixel value of the ROI in the top-left-hand corner of the image. Each ROI was transformed by a two-dimensional FFT and the absolute magnitude squared of each FFT was averaged together to obtain the NNPS. This procedure could be summarized in the following equation:³⁷

$$\text{NNPS}(u,v) = \frac{dA}{M \cdot N^2} \sum_{i=1}^M \left\{ \frac{\langle \text{ROI}_i \rangle}{\langle \text{ROI}_1 \rangle} \left| \text{FFT} \left[\frac{1}{\langle \text{ROI}_i \rangle} (\text{ROI}_i - \langle \text{ROI}_i \rangle) \right] \right|^2 \right\}, \quad (1)$$

where dA represented the pixel area, M described the number of regions of interest in which the image was segmented, N corresponded to the number of pixels along one edge of an ROI, ROI_i referred to a particular region of interest within the flat field image, ROI_1 corresponded to the ROI in the top-left corner of the image, and $\langle \text{ROI}_i \rangle$ was the mean of ROI_i . To summarize this two-dimensional information in one-dimensional form, horizontal and vertical traces were obtained by averaging together the central frequency bands (the central axis and ± 5 frequency lines). Radial traces were also obtained by radial averaging.

The magnitude of the NNPS could be related to the image variance using Parseval's Theorem³⁹ and applying ergodic assumptions. This allowed the replacement of $\langle \text{ROI}_i \rangle$ by $\langle I \rangle$, the mean of the entire image, and the mean variance of the ROIs became the variance of the image, σ^2 . One could then show that

TABLE II. Ideal SNR^2/mR values calculated for an energy-integrating detector. The beams were modeled with the specified intrinsic filtrations as well as the experimentally measured half-value layer.

| Name | Anode target | Anode filtration | $q_{\text{ideal}}(\text{mm}^{-2} \text{mR}^{-1})$ |
|--------|--------------|--------------------------------|---|
| RQA-M2 | Molybdenum | Molybdenum (30 μm) | 46052 |
| RQA-M4 | Molybdenum | Molybdenum (30 μm) | 52542 |
| MW2 | Tungsten | Rhodium (50 μm) | 54773 |
| MW4 | Tungsten | Rhodium (50 μm) | 67781 |

$$\sum_{u,v} \text{NNPS}(u,v) = \frac{N^2 dA}{\langle I \rangle^2} \sigma^2. \quad (2)$$

For a linear, quantum-limited detector, $\langle I \rangle$ and σ^2 are proportional to the exposure, E , which would make the product of the NNPS and exposure independent of exposure. The product of NNPS and exposure was then used as a way to assess how well the detector approximated a quantum-limited detector.

A second examination of system noise utilized a background subtraction method, which isolated the quantum noise components of total system noise.³⁹⁻⁴² An average image was created from ten repeated images acquired with the RQA-M2 technique at 125 mAs. The average image was then subtracted from one of the individual images to form a "background-free" image. The NNPS was then computed from the "background-free" image. To correct for the change in image variance caused by the averaging technique, the NNPS for the "background-free" image was multiplied by $N/(N-1)$, where N equaled 10, the number of images used to create the average image.⁴²

F. Detective quantum efficiency

The measured MTF and NNPS were combined to determine the Detective Quantum Efficiency (DQE) as

$$\text{DQE}(u) = \frac{\text{MTF}^2(u)}{q_{\text{ideal}} \cdot E \cdot \text{NNPS}(u)}, \quad (3)$$

where q_{ideal} described the ideal signal to noise (SNR) ratio squared per unit exposure for an energy-integrating detector, and E represented the exposure value at the detector.^{39,43} An x-ray simulation program (xSpect, Henry Ford Health System) was used to calculate the q_{ideal} using a semiempirical model for the x-ray spectra⁴⁴ and the attenuation properties of the material.³³ The q values are reported in Table II.

G. Image lag measurement

The magnitude of the multiplicative image lag was characterized using the procedure described in IEC standard 62220-1.⁴⁵ First, an image was acquired of a uniform radiation field at a given exposure at time t_1 . A second image was then acquired of an edge device at the same exposure level at time t_2 . After a specified delay time τ , a third image was acquired of a uniform radiation field at time t_3 . This procedure then measured the residual signal from the edge device in the later image.

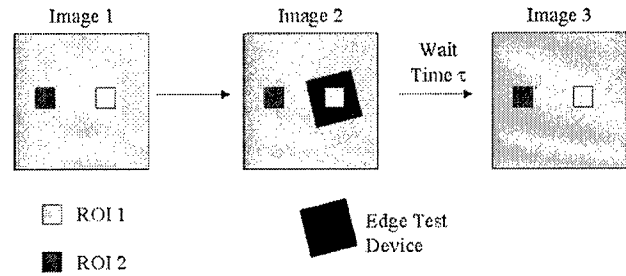


FIG. 2. Illustration of the lag measurement procedure as described in the IEC standard 62220-1.

To determine the magnitude of the residual signal, the image data were examined for two regions within all three images, as shown graphically in Fig. 2. An ROI, ROI₁, was placed in an area of image 2 that contained the edge device. A second ROI, ROI₂, was placed in an area of image 2 that was outside of the edge device. The detector was judged to have negligible residual signal with time delay τ if it passed the following test:⁴⁵

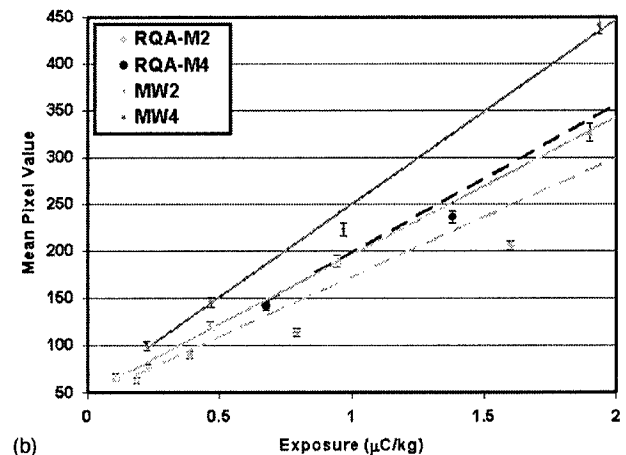
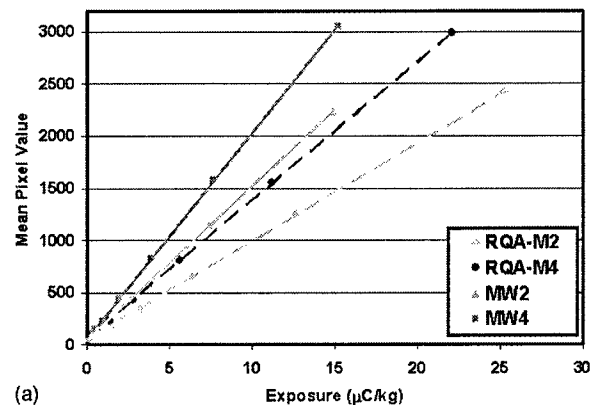


FIG. 3. Plot of mean pixel value versus exposure for two Mo/Mo beams and two W/Rh beams over the (a) entire measured exposure range and (b) the lower exposure range. While the detector exhibits good linearity over the entire range, divergences from linearity occur in the lower exposure range.

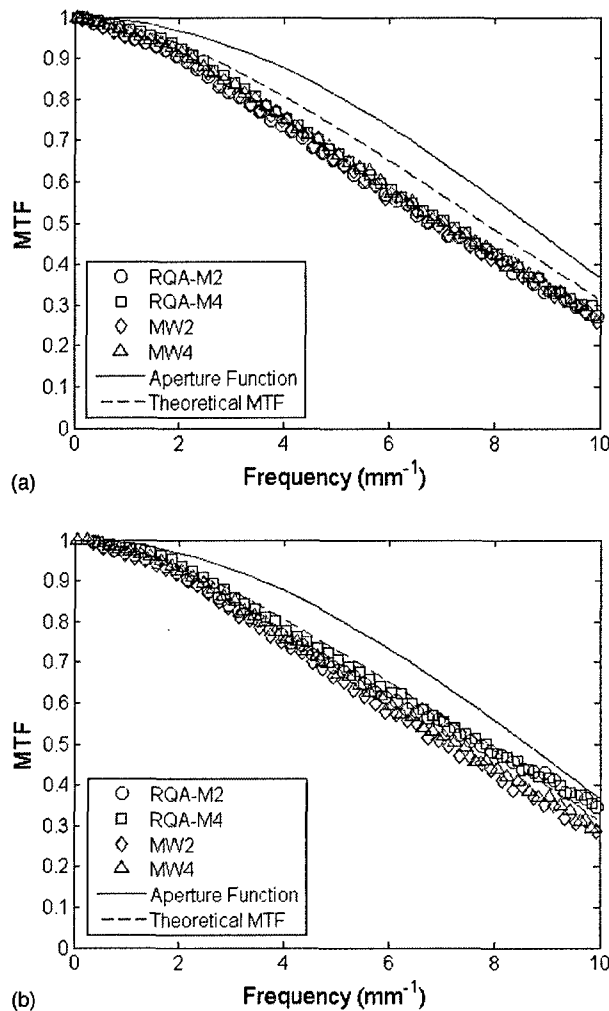


FIG. 4. Plot of detector MTF along (a) CN and (b) LR axes for two Mo/Mo beams and two W/Rh beams. The MTFs for the four beams are very similar for the CN axis, but differ along the LR axis. The pixel aperture limit and theoretical MTF (Ref. 18) are included for reference.

$$\frac{|\zeta_{t_1} - \eta_{t_1} - (\zeta_{t_3} - \eta_{t_3})|}{\frac{\eta_{t_1} + \eta_{t_3}}{2}} \leq 0.005, \quad (4)$$

where ζ_t and η_t represented the mean of ROI₁ and ROI₂ at time t , respectively. The IEC chose the threshold of 0.005 as the maximum allowable level of residual signal.

III. RESULTS

Figure 3 illustrates the relationship between pixel value and exposure for the detector. In general, the system showed a very linear response with correlation coefficients for linear regression fits greater than 0.999. One interesting trend was that the detector was slightly more sensitive to the W/Rh beam qualities than the Mo/Mo beams, as the tungsten curves resulted in higher slopes and higher pixel values for equivalent exposures. Another trend was revealed by exam-

TABLE III. Summary of the detector MTF properties along CN and LR axes for (top) Mo/Mo beams and (bottom) W/Rh beams. Shown are frequencies at specific MTFs and the MTF at specific frequencies. The MTF for the Mo/Mo beams differed between the CN and LR axes, but was similar for the W/Rh beams.

| | RQA-M2 (CN Axis) | RQA-M2 (LR Axis) | RQA-M4 (CN Axis) | RQA-M4 (LR Axis) |
|----------------------|-----------------------|-----------------------|-----------------------|-----------------------|
| 0.2 MTF | 11.1 mm ⁻¹ | 12.7 mm ⁻¹ | 11.2 mm ⁻¹ | 12.5 mm ⁻¹ |
| 0.1 MTF | 12.8 mm ⁻¹ | 14.8 mm ⁻¹ | 12.8 mm ⁻¹ | 14.5 mm ⁻¹ |
| 0.5 mm ⁻¹ | 0.98 | 0.99 | 0.99 | 1.0 |
| 2.5 mm ⁻¹ | 0.86 | 0.88 | 0.89 | 0.90 |
| 5.0 mm ⁻¹ | 0.65 | 0.70 | 0.67 | 0.71 |

| | MW2 (CN Axis) | MW2 (LR Axis) | MW4 (CN Axis) | MW4 (LR Axis) |
|----------------------|-----------------------|-----------------------|-----------------------|-----------------------|
| 0.2 MTF | 11.1 mm ⁻¹ | 11.4 mm ⁻¹ | 11.2 mm ⁻¹ | 11.5 mm ⁻¹ |
| 0.1 MTF | 12.9 mm ⁻¹ | 13.2 mm ⁻¹ | 12.9 mm ⁻¹ | 13.3 mm ⁻¹ |
| 0.5 mm ⁻¹ | 0.98 | 0.99 | 0.99 | 0.99 |
| 2.5 mm ⁻¹ | 0.86 | 0.87 | 0.88 | 0.89 |
| 5.0 mm ⁻¹ | 0.65 | 0.67 | 0.67 | 0.68 |

ining the lower exposure range, such as that shown in Fig. 3(b), where some deviations from linearity were seen.

To verify image repeatability over time, an ensemble of images was acquired at identical mAs. The mean signal for each image was computed as the average pixel value over a region of interest. These images showed very similar signal levels over time, as the mean signal varied by 0.009% over the entire ensemble of images. In contrast, the spatial deviation, which described how the pixel values varied across each image, reached 3.4% for the lowest exposure images.

The resolution properties of the detector, as represented by the MTF, are shown in Fig. 4 and summarized in Table III. Figure 4(a) illustrates the MTF along the CN axis, while Fig. 4(b) displays the MTF along the LR axis. While the MTFs for the tungsten and molybdenum techniques overlapped considerably for the CN direction, the molybdenum

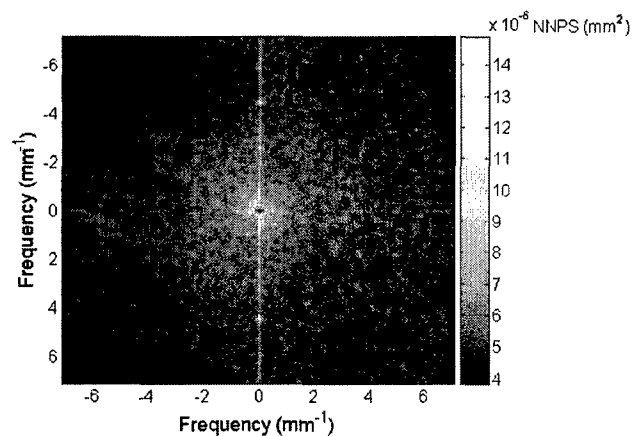


FIG. 5. Two-dimensional NNPS for RQA-M2 beam quality at 1.58 $\mu\text{C}/\text{kg}$ exposure. The image is shown in a logarithmic scale. Nonstochastic noise is observed in a frequency band along the CN frequency axis.

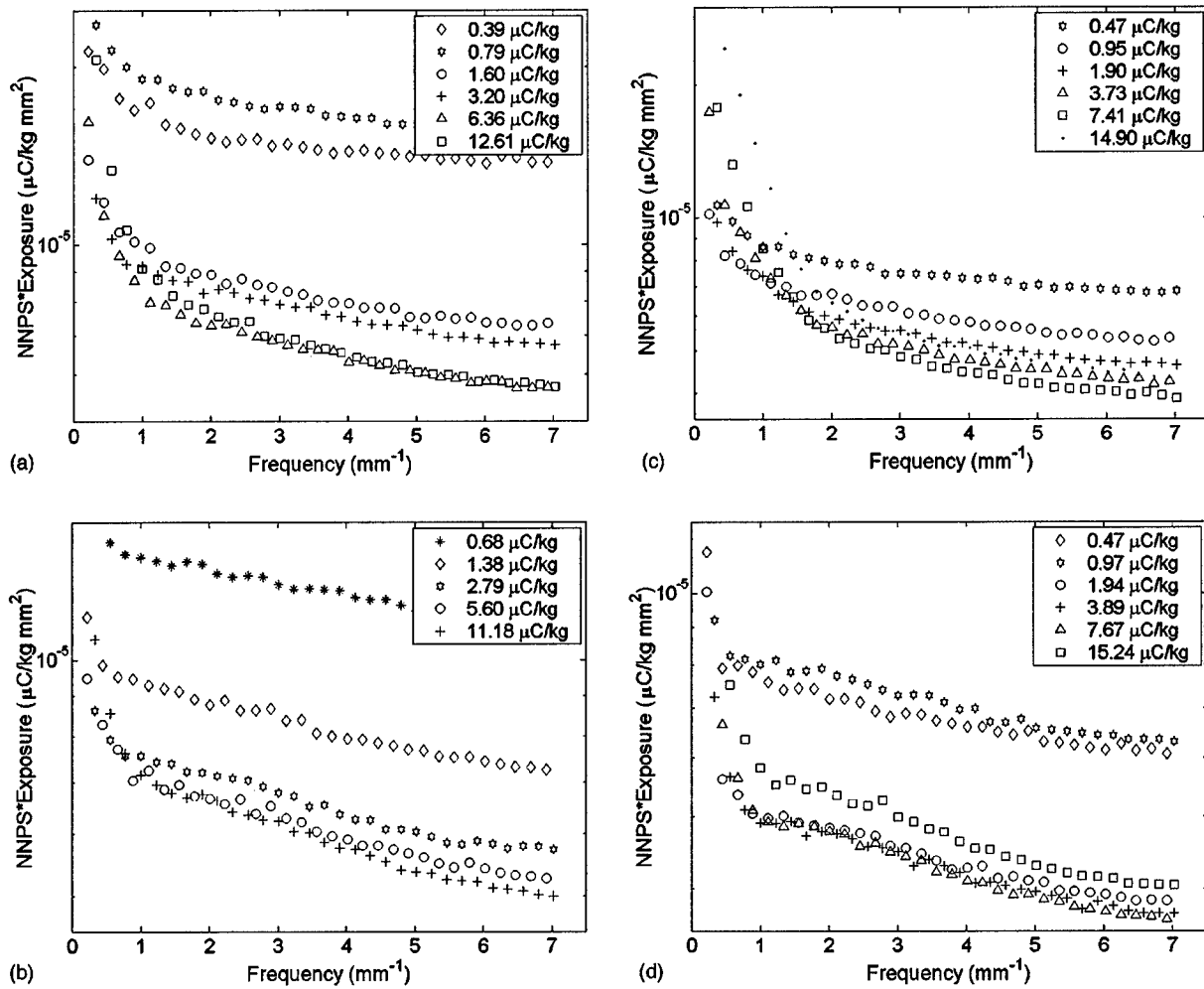


FIG. 6. Radial traces of NNPS multiplied by exposure for (a) RQA-M2, (b) RQA-M4, (c) MW2, and (d) MW4 beam qualities.

and tungsten curves diverged for the LR axis. For reference, Fig. 4 also displays the pixel aperture function and the theoretical limit calculated by Yorker *et al.*¹⁸

Figure 5 shows an example of a two-dimensional NNPS displayed in a logarithmic scale (RQA-M2 technique, 1.58 $\mu\text{C}/\text{kg}$). The figure demonstrates nonstochastic noise in the CN direction along a band of 0.112 mm^{-1} in width. Similar behavior was observed for other exposures and beam qualities. Figure 6 illustrates the radial NNPS multiplied by exposure. As discussed in Sec. II E, the product of NNPS and exposure should remain constant for strictly quantum-limited detectors, however, the results showed notable exposure dependencies. For lower exposures, the magnitude of this metric decreased to some minimum value as one increased exposure. For several techniques, the magnitude of the metric increased at higher exposures.

Figure 7 illustrates the NNPS calculated through the background subtraction method. The background subtraction method noticeably reduced the low-frequency noise. In addition, the overall magnitude of the NNPS decreased. One

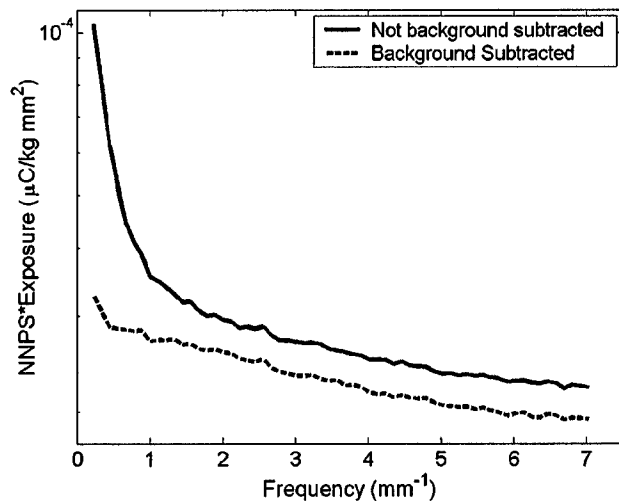


FIG. 7. Radial traces of NNPS multiplied by exposure obtained with and without background subtraction method. The NNPS was obtained using RQA-M2 technique at $12.6 \mu\text{C}/\text{kg}$. The background subtraction routine reduced the low-frequency noise and lowered overall noise.

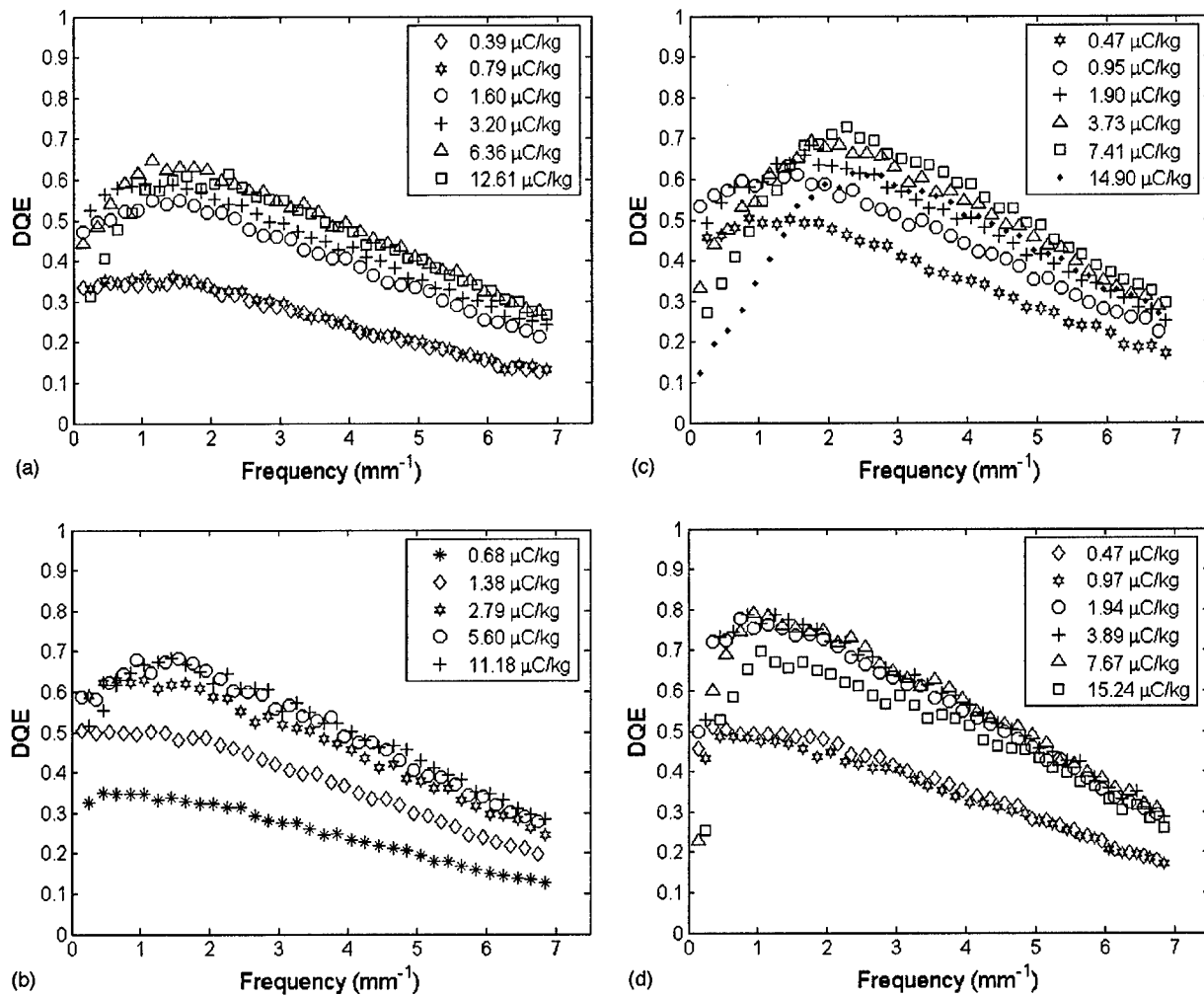


FIG. 8. DQE averaged over CN and LR axes for (a) RQA-M2, (b) RQA-M4, (c) MW2, and (d) MW4 beam qualities.

TABLE IV. Detector DQE along the (top) CN axis and (bottom) LR axes. As the low-frequency noise caused peaks in the DQE, the table reports the maximum DQE value and the frequency at which this maximum occurs.

| | RQA-M2 (1.60 $\mu\text{C/kg}$) | RQA-M4 (2.79 $\mu\text{C/kg}$) | MW2 (1.90 $\mu\text{C/kg}$) | MW4 (1.94 $\mu\text{C/kg}$) | Background subtracted RQA-M2 (12.6 $\mu\text{C/kg}$) |
|-----------------------|------------------------------------|------------------------------------|---------------------------------|---------------------------------|---|
| 0.15 mm^{-1} | 46% | 59% | 46% | 50% | 73% |
| 2.5 mm^{-1} | 49% | 55% | 61% | 66% | 64% |
| 5.0 mm^{-1} | 31% | 36% | 41% | 44% | 44% |
| Peak | 55% | 63% | 66% | 77% | 73% |
| | 1.25 mm^{-1} | 0.85 mm^{-1} | 1.55 mm^{-1} | 0.85 mm^{-1} | 0.15 mm^{-1} |

| | RQA-M2 (1.60 $\mu\text{C/kg}$) | RQA-M4 (2.79 $\mu\text{C/kg}$) | MW2 (1.90 $\mu\text{C/kg}$) | MW4 (1.94 $\mu\text{C/kg}$) | Background subtracted RQA-M2 (12.6 $\mu\text{C/kg}$) |
|-----------------------|------------------------------------|------------------------------------|---------------------------------|---------------------------------|---|
| 0.15 mm^{-1} | 47% | 59% | 47% | 52% | 77% |
| 2.5 mm^{-1} | 50% | 57% | 61% | 70% | 68% |
| 5.0 mm^{-1} | 34% | 41% | 41% | 47% | 49% |
| Peak | 53% | 63% | 63% | 77% | 77% |
| | 1.45 mm^{-1} | 0.95 mm^{-1} | 1.85 mm^{-1} | 0.85 mm^{-1} | 0.15 mm^{-1} |

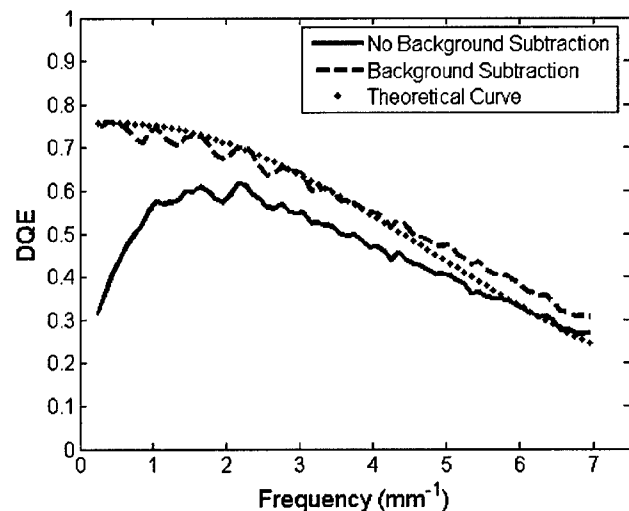


FIG. 9. DQE calculated using background subtraction method averaged over the CN and LR axes. The DQE was computed for RQA-M2 technique at $12.6 \mu\text{C}/\text{kg}$. The background subtraction routine reduced the low frequency peaking. The plot also shows a theoretical estimation of the DQE (Ref. 46) for a similar detector ($200 \mu\text{m}$ selenium layer, $85 \mu\text{m}$ pixel size).

should note that the noise was corrected for the change in noise variance due to the subtraction technique, as discussed in Sec. II E.

Figure 8 shows the DQE measured for all techniques in the axial (the average of CN and LR axes) direction. The DQE curves showed low frequency peaking, in that the DQE exhibited a sharp increase at lower frequencies. The strong low-frequency component of the NNPS led to this unusual behavior. Moreover, the DQE increased with exposure for lower exposure values, reached a peak value, and then decreased for higher exposures. This was also expected from the behavior of the NNPS. The DQE is summarized in Table IV for all four techniques along both CN and LR axes.

To separate the fixed pattern noise from quantum noise effects, the DQE was calculated with the background subtraction method. Figure 9 illustrates the DQE computed with this method in the axial direction. By eliminating the fixed pattern noise, the low-frequency peaking in the DQE was removed and the overall efficiency increased. This figure also includes the theoretical DQE calculated for a similar detector for reference ($200 \mu\text{m}$ selenium layer, $85 \mu\text{m}$ pixel size).⁴⁶

The results from lag measurements are summarized in Table V. In general, the image lag for the detector passed the test established by IEC 62220-1. An interesting phenomenon occurred for the fourth test ($75 \mu\text{Gy}$ exposure, 5 min decay time). The residual signal level was unacceptably high for this test, even though a similar test ($75 \mu\text{Gy}$ exposure, 3 min decay time) produced acceptable levels of residual signal.

IV. DISCUSSION

Digital mammography has begun to replace screen-film systems in some clinical settings. The motivation for this change includes several logistical considerations, such as

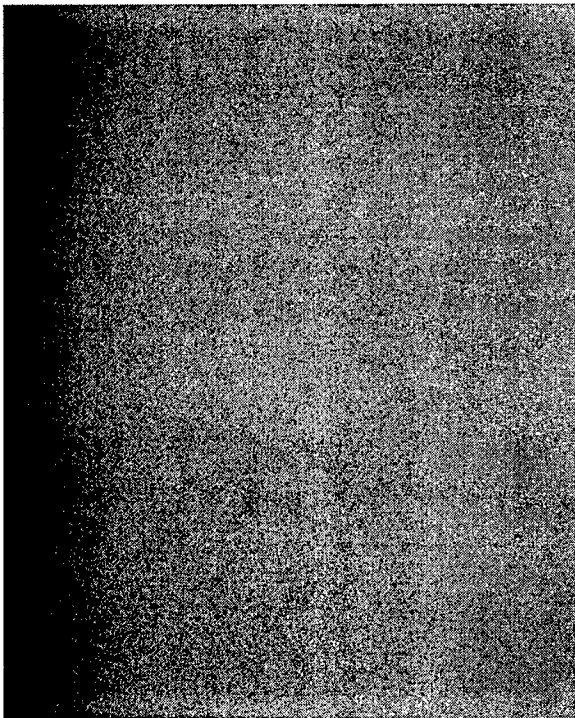
TABLE V. Lag properties of the detector. The lag tests were executed in the order shown in the table, with the top three rows measuring signal retention after a 3 min decay time, then a gap of 10 mins, and the bottom three rows measured signal retention after a 5 min delay time. The metric corresponded to IEC 62220-1 with values less than 0.005 acceptable under the IEC guidelines.

| Test Number | Exposure (μGy) | Decay time (min) | Metric | Acceptable residual signal? |
|-----------------|-----------------------------|------------------|--------|-----------------------------|
| 1 | 75 | 3 | 0.002 | Yes |
| 2 | 150 | 3 | 0.0048 | Yes |
| 3 | 200 | 3 | 0.0044 | Yes |
| Ten minute wait | | | | |
| 4 | 75 | 5 | 0.047 | No |
| 5 | 150 | 5 | 0.013 | No |
| 6 | 200 | 5 | 0.0022 | Yes |

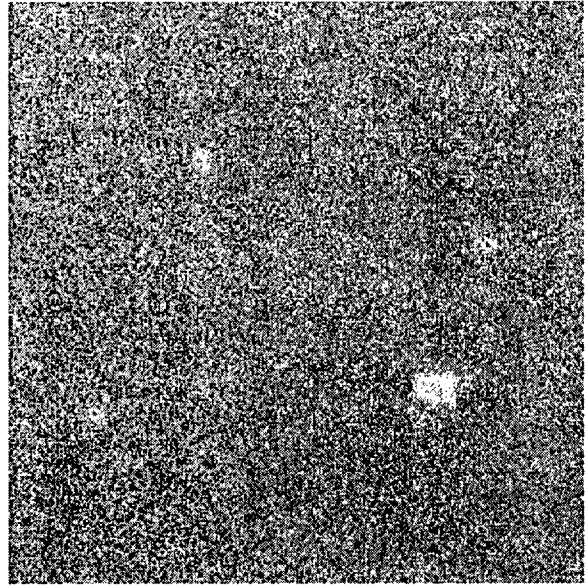
convenient archiving and display, and potential image quality advantages. The two flat-panel technologies currently offered, direct and indirect, vary markedly in terms of their image quality characteristics. Direct detectors tend to enjoy higher resolution than indirect detectors. However, they are often less efficient than their indirect counterparts.^{9,10} In this study, we evaluated all physical properties of a particular direct flat-panel detector, including resolution, noise, and efficiency, to enable a thorough comparison between that detector and others.

Several other investigators have examined the physical characteristics of flat-panel mammographic imagers. As such, the results from this system characterization must be reported in the context of the performance of other systems. When considering previous measurements, one should note any differences in beam energies and filtrations. Most prior studies utilized molybdenum anodes with molybdenum filtration at 28 kVp, but often utilized a breast equivalent phantom for further filtration.^{18,46-49} While this should still allow for reasonable comparisons between MTFs, these differences would make comparisons of DQE curves more challenging.

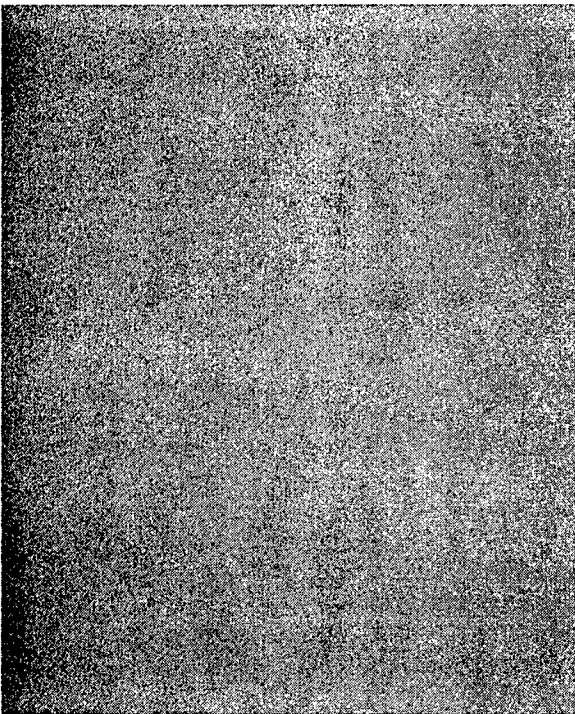
Compared to previous measurements of indirect flat-panel imagers,^{47,48} the current system exhibited a higher MTF. At low frequencies, our MTF was similar to other direct flat-panel imagers, but our MTF was higher at higher frequencies.^{46,49} As the pixel size served as the primary limiter of the resolution of a direct detector, with some blurring effects from backscatter and reabsorption of K x-rays, the similarity between direct detectors was reasonable. At similar exposures, the DQE of the system was generally higher than that of indirect flat-panel imagers, although the low-frequency peaking complicated this comparison.⁴⁷ In comparison to the work by Jee, the High Light (HL) output configuration produced a higher DQE but the High Resolution (HR) configuration appeared to produce a lower DQE than our current system.⁴⁸ The direct detector evaluated by Zhao produced a generally higher DQE, with constant behavior for different exposures, although there were significant differences between the axes.⁴⁶ One interesting result was that



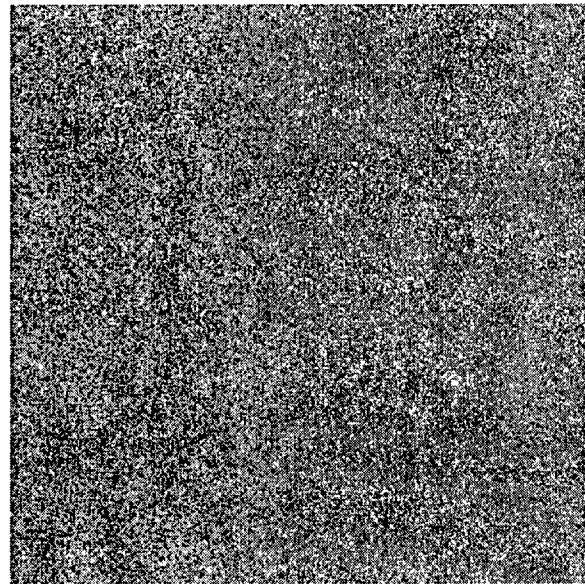
(a)



(c)



(b)



(d)

FIG. 10. Example image of uniform beam of radiation (a) before and (b) after the application of a secondary gain correction from the average of 10 images. The larger images (physical size: 23.3 cm \times 28.7 cm) show the differences in large-scale gain nonuniformities. Zoomed portion of the images (2.1 cm \times 2.1 cm) highlighting pixel artifacts (c) before and (d) after gain calibration. The gain calibration largely removes the pixel artifacts from the individual images.

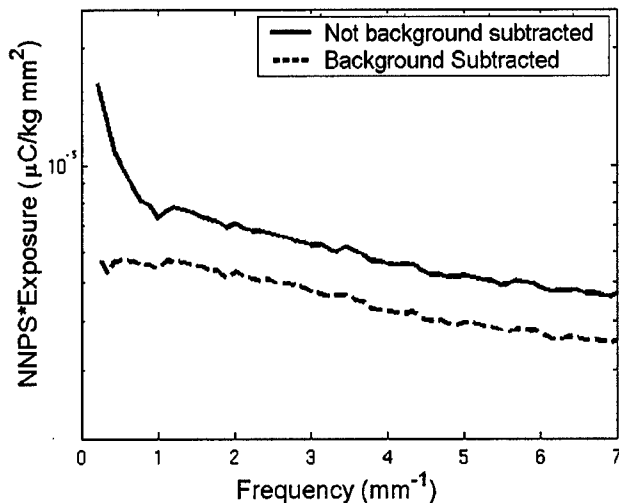


FIG. 11. Radial traces of NNPS multiplied by exposure obtained with and without background subtraction method for a second prototype detector. The NNPS was obtained using RQA-M2 technique at $7.67 \mu\text{C}/\text{kg}$. As with the prototype system, this detector unit also exhibits significant stochastic noise.

some previous studies on selenium detector systems^{46,49} have also observed some low-frequency peaking in the DQE, although it was less pronounced than that observed in this study.

Yorker *et al.* have published the MTF and DQE measurements of a similar mammographic detector with an identical pixel size.¹⁸ That study examined the MTF and DQE for one radiographic technique using a molybdenum anode operated at 28 kVp with molybdenum filtration. The reported MTF for this technique was very similar to our measured MTF acquired at the RQA-M2 technique. At similar exposures, our DQE acquired at RQA-M2 also appeared comparable to that of Yorker *et al.* However, given the fact that Yorker *et al.* used a 4.2 cm breast phantom filter in the beam, quantitative comparisons are not straightforward.

Several researchers have explored the theoretical properties of selenium-based flat-panel imagers operated at mammographic energies. The properties of this system compared favorably with these theoretical calculations. As shown in Figs. 4(a) and 4(b), the MTF of this system remained close to the theoretical limit, as calculated by Yorker *et al.*¹⁸ When using the background subtraction method to remove fixed pattern noise, the DQE of the system appeared similar to its theoretical value for a similar detector.⁴⁶ The difference between the theoretical and experimental values were likely due to the assumptions behind the theoretical calculation, which assumed a 200 μm selenium layer and 85 μm pixel size. These theoretical calculations should underestimate the actual detector efficiency, as a larger selenium layer will more efficiently capture x-ray photons and a smaller pixel size should boost the higher frequency portions of the DQE. Notwithstanding, the experimental results for the MTF and DQE largely agreed with their theoretical values.

This prototype detector had very favorable resolution properties, as shown by its MTF. There was an asymmetry in the MTF, however, as the tungsten and molybdenum curves

overlapped for the CN axis but diverged for the LR axis. The difference might be attributed to the differences between the focal spots for the two anodes, in terms of both shape and location. The impact of focal spot blur should be minimal as the edge was placed directly on the detector. Further work remains needed to evaluate the focal spot properties for both anode varieties and to determine whether this phenomenon occurs with different tubes.

The prototype detector did show significant structured noise contributions. This could be decomposed into two factors: (a) low frequency trending over the image and (b) pixel artifacts. The trending was expressed as a strong low-frequency component of the NNPS. In contrast, pixel artifacts were similar to delta functions and elevated all frequencies of the NNPS. A background subtraction method eliminated both of these factors, so one was unable to determine the relative magnitude of either individually. Therefore, when one compared the NNPS calculated using the background-subtraction technique to that calculated using standard techniques, one noticed a decrease in the low-frequency noise contribution as well as an overall decrease in the magnitude of the NNPS. This was reflected in the DQE as well. When the DQE was calculated using background-subtraction techniques, the sharp low-frequency drop was eliminated and the overall curve was shifted upwards because of the decrease in noise.

Several of these noise concerns could be mitigated by additional gain calibration after the gain calibration performed by the system. To examine the benefits of further gain calibration, a gain map was created by averaging ten uniform images together. This gain map was then applied to a subsequently acquired image. The effect of the gain calibration is shown in Fig. 10 and displayed with identical window and level settings. The prominent trending was greatly diminished and many of the pixel artifacts were eliminated. To assess whether the problem observed was unique to the prototype detector tested, a follow-up experiment was conducted on a more recent prototype device to learn whether it exhibited noise properties similar to the earlier prototype. This experiment compared the NNPS calculated with and without the background subtraction methodology, as shown in Fig. 11. The background subtraction proved to similarly remove significant nonuniformities, which indicated that the images after system gain calibration retained substantial structured noise in the second prototype as well.

The detector was evaluated for four different beam qualities. Two beams used a molybdenum anode with molybdenum filtration and two used a tungsten anode with rhodium filtration. The tungsten beam qualities were developed specifically for this study and inspired by IEC standards. The detector appeared to be slightly more sensitive to the tungsten beams, as shown in the exposure-pixel value relationship. Moreover, the DQEs for the tungsten beams were higher than those for the molybdenum beams, although this was obscured by the peaking in the DQE curves. This suggests that tungsten beams might produce higher quality images with digital detectors than the traditional molybdenum beams.

Using the parameters established by IEC 62220-1, the image lag appeared within reasonable parameters. Nevertheless, high exposures led to unusual behavior in signal retention, affecting other exposures even after a significant length of time. Ten minutes before the fourth lag test (75 μGy exposure, 5 min decay time), a 200 μGy lag test was conducted. It appeared that this high exposure still affected the detector after 10 mins, as a 75 μGy exposure should not have higher residual signal after a 5 min decay time than it would after a 3 min decay time. The mechanisms for this behavior are unknown and suggest additional investigation into signal retention properties of selenium.

V. CONCLUSIONS

This study reported an assessment of image quality for a prototype mammographic imager based on a direct-detection, flat-panel array employing an amorphous selenium converter. The results indicated that the detector had strong potential for capturing high-frequency information, as exhibited by its high MTF. In addition, the DQE of the detector approached the high value of 75%–80%. Yet, suboptimal calibration affected the DQE performance of the system, underscoring the importance of careful gain and dead pixel corrections in reducing detector nonuniformities. Finally, this study introduced two new radiographic techniques utilizing tungsten anodes for the assessment of mammographic systems, which will facilitate the future comparisons of detector characteristics operated with tungsten anodes.

ACKNOWLEDGMENTS

The authors would like to thank Jim Dobbins and Carey Floyd of Duke University for several helpful conversations and Thomas Mertelmeier of Siemens Medical Solutions for his assistance with this project. This work was partially supported by a grant from Siemens Medical Solutions and USAMRMC W81XWH-04-1-0323.

¹American Cancer Society, *Cancer Facts and Figures 2004* (American Cancer Society, Atlanta, GA, 2004).

²I. Jatoi, "Breast cancer screening," *Am. J. Surg.* **177**, 518–524 (1999).

³K. Kerlikowske, D. Grady, S. M. Rubin, C. Sandrock, and V. L. Ernster, "Efficacy of screening mammography: A meta-analysis," *J. Am. Med. Assoc.* **273**, 149–154 (1995).

⁴R. E. Bird, T. W. Wallace, and B. C. Yankaskas, "Analysis of cancers missed at screening mammography," *Radiology* **184**, 613–617 (1992).

⁵E. D. Pisano, "Current status of full-field digital mammography," *Radiology* **214**, 26–28 (2000).

⁶L. Fajardo and M. Williams, "The clinical potential of digital mammography," in *Digital Mammography '96*, edited by K. Doi, M. Giger, R. Nishikawa, and R. Schmidt (Elsevier, New York, 1996), pp. 43–52.

⁷A. Maidment and M. Yaffe, "Scanned-slot digital mammography," *Proc. SPIE* **1231**, 316–326 (1990).

⁸M. J. Yaffe and J. A. Rowlands, "X-ray detectors for digital radiography," *Phys. Med. Biol.* **42**, 1–39 (1997).

⁹E. Samei and M. J. Flynn, "An experimental comparison of detector performance for direct and indirect digital radiography systems," *Med. Phys.* **30**, 608–622 (2003).

¹⁰E. Samei, M. J. Flynn, H. G. Chotas, and J. T. Dobbins, III, "DQE of direct and indirect digital radiographic systems," *Proc. SPIE* **4320**, 189–197 (2001).

¹¹W. Zhao, I. Blevis, S. Germann, J. A. Rowlands, D. Waechter, and Z. S. Huang, "Digital radiology using active matrix readout of amorphous se-

lenium: Construction and evaluation of a prototype real-time detector," *Med. Phys.* **24**, 1834–1843 (1997).

¹²D. L. Lee, L. K. Cheung, B. Rodricks, and G. F. Powell, "Improved imaging performance of a 14×17-inch direct radiography [trademark] system using Se/TFT detector," *Proc. SPIE* **3336**, 14–23 (1998).

¹³J. A. Rowlands and J. Yorkston, "Flat panel detectors for digital radiography," in *Handbook of Medical Imaging*, edited by H. K. J. Beutel, H. L. Kundel, and R. Van Metter (SPIE, Washington, D.C., 2000), Vol. 1, pp. 223–328.

¹⁴J. H. Siewerdsen, L. E. Antonuk, Y. El-Mohri, J. Yorkston, W. Huang, and I. A. Cunningham, "Signal, noise power spectrum, and detective quantum efficiency of indirect-detection flat-panel imagers for diagnostic radiology," *Med. Phys.* **25**, 614–628 (1998).

¹⁵Y. El-Mohri, L. E. Antonuk, K.-W. Jee, Y. Kang, Y. Li, A. Sawant, Z. Su, Y. Wang, J. Yamamoto, and Q. Zhao, "Evaluation of novel direct- and indirect-detection active matrix flat-panel imagers (AMFPIs) for mammography," *Proc. SPIE* **5030**, 168–180 (2003).

¹⁶K.-W. Jee, L. E. Antonuk and Y. El-Mohri, "Evaluation of direct-detection and indirect-detection active matrix, flat-panel imagers (AMFPIs) for digital mammography," *Proc. SPIE* **4320**, 13–23 (2001).

¹⁷R. S. Saunders Jr., E. Samei, J. Y. Lo, and J. L. Jesneck, "Physical characterization of a selenium-based full field digital mammography detector," *7th International Workshop on Digital Mammography*, 2004.

¹⁸J. G. Yorker, L. S. Jeromin, D. L. Y. Lee, E. F. Palecki, K. P. Golden, and Z. Jing, "Characterization of a full-field digital mammography detector based on direct x-ray conversion in selenium," *Proc. SPIE* **4682**, 21–29 (2002).

¹⁹H. Fujita, K. Doi, and M. L. Giger, "Investigation of basic imaging properties in digital radiography 6. MTFs of II-TV digital imaging-systems," *Med. Phys.* **12**, 713–720 (1985).

²⁰M. Spahn, M. Strotzer, M. Volk, S. Bohm, B. Geiger, G. Hahn, and S. Feuerbach, "Digital radiography with a large-area, amorphous-silicon, flat-panel x-ray detector system," *Invest. Radiol.* **35**, 260–266 (2000).

²¹C. D. Bradford, W. W. Pepler, and J. M. Waidelich, "Use of a slit camera for MTF measurements," *Med. Phys.* **26**, 2286–2294 (1999).

²²M. B. Williams, P. A. Mangiafico, and P. U. Simoni, "Noise power spectra of images from digital mammography detectors," *Med. Phys.* **26**, 1279–1293 (1999).

²³A. D. A. Maidment and M. J. Yaffe, "Analysis of the spatial-frequency-dependent DQE of optically coupled digital mammography detectors," *Med. Phys.* **21**, 721–729 (1994).

²⁴A. Workman and D. S. Brettle, "Physical performance measures of radiographic imaging systems," *Dentomaxillofac Radiol.* **26**, 139–146 (1997).

²⁵W. Zhao, G. DeCrescenzo, and J. A. Rowlands, "Investigation of lag and ghosting in amorphous selenium flat-panel x-ray detectors," *Proc. SPIE* **4682**, 9–20 (2002).

²⁶M. Yaffe, "Digital mammography," in *Handbook of Medical Imaging*, edited by H. K. J. Beutel and R. V. Metter (SPIE, Washington, D.C., 2000), Vol. 1, pp. 329–372.

²⁷R. Fahrig and M. J. Yaffe, "Optimization of spectral shape in digital mammography: Dependence on anode material, breast thickness, and lesion type," *Med. Phys.* **21**, 1473–1481 (1994).

²⁸R. L. McKinley, M. P. Tornai, E. Samei, and M. L. Bradshaw, "Simulation study of a quasi-monochromatic beam for x-ray computed mammotomography," *Med. Phys.* **31**, 800–813 (2004).

²⁹E. A. Berns, R. E. Hendrick, and G. R. Cutter, "Optimization of technique factors for a silicon diode array full-field digital mammography system and comparison to screen-film mammography with matched average glandular dose," *Med. Phys.* **30**, 334–340 (2003).

³⁰D. R. Dance, A. K. Thilander, M. Sandborg, C. L. Skinner, I. A. Castellano, and G. A. Carlsson, "Influence of anode/filter material and tube potential on contrast, signal-to-noise ratio and average absorbed dose in mammography: A Monte Carlo study," *Br. J. Radiol.* **73**, 1056–1067 (2000).

³¹L. K. Wagner, B. R. Archer, and F. Cerra, "On the measurement of half-value layer in film-screen mammography," *Med. Phys.* **17**, 989–997 (1990).

³²International Electrotechnical Commission, *Medical diagnostic x-ray equipment-Radiation conditions for use in the determination of characteristics* (IEC-61267, Geneva, Switzerland, 2003).

³³E. Samei and M. J. Flynn, "An experimental comparison of detector performance for computed radiography systems," *Med. Phys.* **29**, 447–459 (2002).

- ³⁴E. Samei, "Image quality in two phosphor-based flat panel digital radiographic detectors," *Med. Phys.* **30**, 1747–1757 (2003).
- ³⁵E. Samei, M. J. Flynn, and D. A. Reimann, "A method for measuring the presampled MTF of digital radiographic systems using an edge test device," *Med. Phys.* **25**, 102–113 (1998).
- ³⁶M. J. Flynn and E. Samei, "Experimental comparison of noise and resolution for 2k and 4k storage phosphor radiography systems," *Med. Phys.* **26**, 1612–1623 (1999).
- ³⁷R. S. Saunders and E. Samei, "A method for modifying the image quality parameters of digital radiographic images," *Med. Phys.* **30**, 3006–3017 (2003).
- ³⁸M. J. Flynn, E. Samei, and D. A. Reimann, "Experimental comparison of noise and resolution for 2K and 4K storage phosphor chest radiography systems," *Radiology* **201**, 1082–1082 (1996).
- ³⁹J. Dobbins, "Image quality metrics for digital systems," in *Handbook of Medical Imaging*, edited by H. K. J. Beutel and R. V. Metter (SPIE, Washington, D.C., 2000), Vol. 1, pp. 163–222.
- ⁴⁰M. L. Giger, K. Doi, and C. E. Metz, "Investigation of basic imaging properties in digital radiography 2. Noise wiener spectrum," *Med. Phys.* **11**, 797–805 (1984).
- ⁴¹P. R. Granfors and R. Aufrichtig, "Performance of a 41×41 -cm² amorphous silicon flat panel x-ray detector for radiographic imaging applications," *Med. Phys.* **27**, 1324–1331 (2000).
- ⁴²R. J. Warp and J. T. Dobbins, "Quantitative evaluation of noise reduction strategies in dual-energy imaging," *Med. Phys.* **30**, 190–198 (2003).
- ⁴³J. C. Dainty and R. Shaw, *Image Science: Principles, Analysis and Evaluation of Photographic-Type Imaging Processes* (Academic, New York, 1974).
- ⁴⁴E. Storm, "Calculated bremsstrahlung spectra from thick tungsten targets," *Phys. Rev. A* **5**, 2328 (1972).
- ⁴⁵International Electrotechnical Commission, *Medical electrical equipment — Characteristics of digital x-ray imaging devices — Part 1: Determination of the detective quantum efficiency (IEC 62220-1, Geneva, Switzerland, 2003)*.
- ⁴⁶W. Zhao, W. G. Ji, A. Debie, and J. A. Rowlands, "Imaging performance of amorphous selenium based flat-panel detectors for digital mammography: Characterization of a small area prototype detector," *Med. Phys.* **30**, 254–263 (2003).
- ⁴⁷S. Vedantham, A. Karellas, S. Suryanarayanan, D. Albagli, S. Han, E. J. Tkaczyk, C. E. Landberg, B. Opsahl-Ong, P. R. Granfors, I. Levis, C. J. D'Orsi, and R. E. Hendrick, "Full breast digital mammography with an amorphous silicon-based flat panel detector: Physical characteristics of a clinical prototype," *Med. Phys.* **27**, 558–567 (2000).
- ⁴⁸K. W. Jee, L. E. Antonuk, Y. El-Mohri, and Q. H. Zhao, "System performance of a prototype flat-panel imager operated under mammographic conditions," *Med. Phys.* **30**, 1874–1890 (2003).
- ⁴⁹B. Lazzari, G. Belli, C. Gori, and K. Nykanen, "Physical characteristics of a clinical prototype for full-field digital mammography with an α -Se flat panel detector," *Proc. SPIE* **5030**, 656–666 (2003).

Effect of Display Resolution on the Detection of Mammographic Lesions

Robert S Saunders, Jr.^{a,b}, Ehsan Samei^{a,b,c}, Jeffrey Johnson,^d Jay Baker^a

^a Duke Advanced Imaging Labs, Department of Radiology, Duke University Medical Center

^b Department of Physics, Duke University

^c Department of Biomedical Engineering, Duke University

^d Siemens Corporate Research

ABSTRACT

For diagnosis of breast cancer by mammography, the mammograms must be viewed by a radiologist. The purpose of this study was to determine the effect of display resolution on the specific clinical task of detection of breast lesions by a human observer. Using simulation techniques, this study proceeded through four stages. First, we inserted simulated masses and calcifications into raw digital mammograms. The resulting images were processed according to standard image processing techniques and appropriately windowed and leveled. The processed images were blurred according to MTFs measured from a clinical Cathode Ray Tube display. JNDMetrix, a Visual Discrimination Model, examined the images to estimate human detection. The model results suggested that detection of masses and calcifications decreased under standard CRT resolution. Future work will confirm these results with human observer studies. (This work was supported by grants NIH R21-CA95308 and USAMRMC W81XWH-04-1-0323.)

Keywords: Image Quality, Mammography, Simulation, Task-Based Assessment

1. INTRODUCTION

After a digital mammogram has been acquired, a human observer must view the data in order to detect or diagnose disease. The display device, therefore, assumes a crucial role in the imaging chain. While several researchers have given significant attention to the quality of image acquisition,¹⁻⁹ fewer investigators have measured the impact of display devices.¹⁰⁻¹³ To understand this impact, studies must evaluate the physical properties of these devices. However, while physical characterization remains important, display quality must ultimately be described in terms of the clinical task in question.¹⁴⁻¹⁶ This study considered this type of question, examining the impact of display resolution on the detection of mammographic lesions.

A Cathode Ray Tube (CRT) display serves as a common mammographic display device.¹⁷ As a CRT ages, its resolution becomes progressively more degraded, leading to lower display quality over time.¹⁸ The purpose of this study was to consider how this degradation in resolution impacted the clinical utility of a CRT display, specifically the detection of breast masses and calcifications.

2. METHODS AND MATERIALS

In this study, first simulated masses and calcifications were inserted into digital mammograms. We applied basic image processing techniques to these images and adjusted the window and level appropriately. Next, we blurred the images according to three different resolution settings measured from a CRT display. Finally, a model observer viewed each of these images to estimate the detection probabilities under each blur setting. The following describes the details of these steps.

2.1 Acquisition of Digital Mammographic Backgrounds

Digital mammographic images were acquired on a clinical flat-panel cesium iodide-based digital mammography system (Senographe 2000D, GE Medical Systems, Milwaukee, WI). Previous studies have characterized the

physical characteristics of this digital mammography system.^{19, 20} Images used in this study were normal craniocaudal view mammograms acquired with a molybdenum anode with molybdenum or rhodium filtration. The beam energies for the images ranged from 25 to 30 kVp and compressed breast thicknesses extended from 2.7 cm to 7.3 cm with varying glandular and adipose tissue composition.

2.2 Lesion Simulation

Simulated breast lesions were placed in the center of mammographic images using an established procedure for simulating masses and calcifications with attributes similar to those of real mammographic lesions.^{21, 22} Breast mass simulation proceeded through three stages, as illustrated in Figure 1. The first stage sets each pixel of an array to its equivalent major axis value,

$$b = \sqrt{[(y - y_0)\cos[\alpha] - (x - x_0)\sin[\alpha]]^2 + \frac{1}{c^2} [(x - x_0)\cos[\alpha] + (y - y_0)\sin[\alpha]]^2} \quad (1)$$

where (x_0, y_0) represent the center of the mass, α determines the angular orientation of the mass, and c corresponds to the ratio of the minor axis length to the major axis length. The second stage introduced non-uniformities in the mass border by multiplying the elliptical rings with a border deviation profile with a given variance and power spectrum. The final stage converted the equivalent major axis values to detector gray level values through the elliptical trace function.

The calcification procedure similarly required three stages. The first stage established the distribution of calcifications, using either a clustered or linear distribution. The second stage created individual calcification at each point specified by the calcification distribution through a series of morphological thickening and erosion operations. This resulted in a binary mask of the calcifications. The final stage added the binary mask to a background image with the appropriate contrast.

The spatial parameters for the simulation routine were determined from screen-film mammographic data obtained through the Digital Database of Screening Mammography.²³ These parameters remained applicable to digital mammographic backgrounds. However, the lesion contrast must be separately calculated for the digital case as the contrast in screen-film images were impacted by varying H&D characteristics. To determine the appropriate contrast for the simulated lesions, the xSpect x-ray simulation program²⁴ calculated the unit contrast for both masses and calcifications embedded in a 50% glandular/50% adipose breast imaged with a cesium-iodide detector. The contrasts were calculated for a molybdenum anode with molybdenum or rhodium filtration for each kVp and breast thickness. Contrast reduction by scattered radiation was also accounted for using previously published measurements.²⁵ The lesions were then inserted in mammographic backgrounds with the appropriate contrast and spatial features for the given anode, filtration, kVp, and breast thickness.

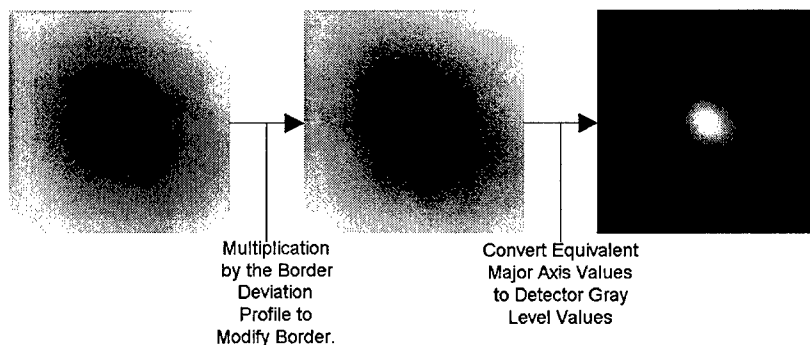


FIG. 1 Schematic of mass simulation procedure. The three images illustrate the three steps in this system.

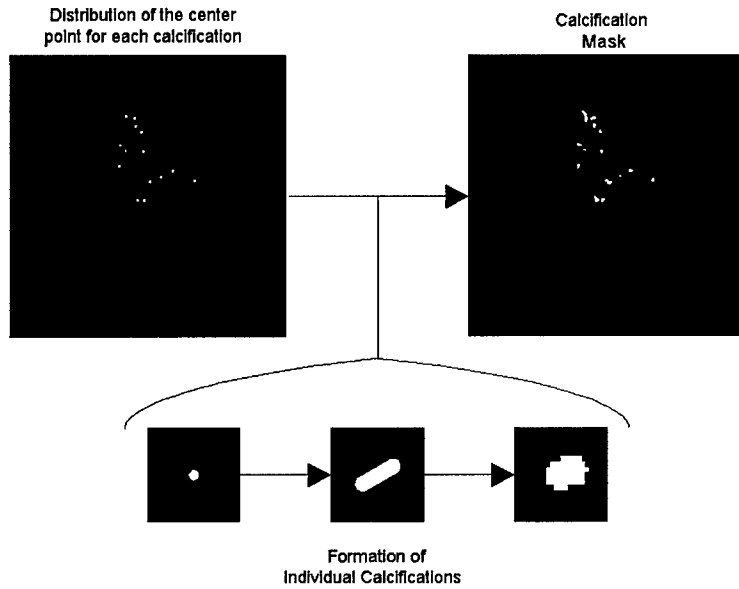


FIG. 2 Illustration of calcification simulation routine. This procedure considers each point in the distribution and creates a unique calcification on each point.

2.3 Image Processing

Most digital mammography systems employ post-processing algorithms to improve image display. A common technique separates the images into multiple frequency bands to improve contrast for specific frequencies. This study utilized a basic image processing algorithm that enhanced two frequency bands in the image.²⁶ The first stage augmented the higher frequency content of the image, while the second stage strengthened the content variations. The parameters for each stage were determined by visual analysis of the images. The first stage accentuated the sharp detail in the image through an unsharp masking procedure as,

$$I_{US} = I + SF(c) \cdot (I - \Sigma \otimes I) \quad (2)$$

where I represented the input image, Σ , the Gaussian kernel, had a standard deviation of 0.45 mm and width of 2.8 mm, and $SF(c)$, the sharpness factor, controlled the level of enhancement. To boost low contrast objects, a non-linear function was utilized for $SF(c)$ as,

$$SF(c) = \begin{cases} G \cdot \left(1 - \frac{c}{c_0}\right)^p + SF_0 & c \leq c_0 \\ SF_0 & c > c_0 \end{cases} \quad (3)$$

with a gain, G , of 1, a contrast threshold, c_0 , of 70, a contrast, c , equal to the absolute difference between the blurred image and original image, and a slope parameter, p , of 3. The second stage enhanced the mid-frequency components of the image, as

$$I_{Out} = (\xi \otimes I_{US}) + CF(c) \cdot (I_{US} - \xi \otimes I_{US}) \quad (4)$$

where ξ represented a Gaussian kernel with a standard deviation of 4.4 mm and $CF(c)$ controlled the level of contrast enhancement. The function $CF(c)$ had the same functional form as $SF(c)$, but utilized a gain, G , of 1.3.

Once the images were processed, observers window and level an image in order to produce an acceptable image appearance. To determine the window and level parameters for each mammogram, an experienced mammographer windowed and leveled each mammogram individually. A sigmoid transformation was fit to each window and level function, to provide a smooth transition at the extremes of the display pixel values. This transformation was represented as

$$I_{Final} = \alpha \left(1 - \frac{1}{1 + e^{-(\text{Log}[I_{Out}] - \delta) / \sigma}} \right) \quad (5)$$

where I_{Out} represented the processed mammogram, δ equaled the center of the sigmoid transition, and σ established the slope of the sigmoid transition.

2.4 Measurement of Display Characteristics

We measured the resolution properties of a five mega-pixel Cathode Ray Tube (CRT) display system (Barco MGD-521, p45 phosphor) with a 10-bit graphics controller (Barco 5MP1H). A charge-coupled device (CCD) camera (XCD-SX900, Sony Corporation, Tokyo, Japan) equipped with a macro lens (Rodgen 1:4, 28mm, Rodenstock, Munich, Germany) acquired images of line test patterns presented on the display. Two images from the recent TG18 test pattern set (TG18-RV50 and TG18-RH50) supplied a vertical and horizontal line, respectively.^{27, 28} To remain in the quasi-linear range of the display, these patterns employed subtle lines, with 12% contrast from the background. We then computed the MTF from these line patterns using established methods. Full details of the measurement methodology has been reported in another publication.²⁹ We measured the MTF for the standard display resolution setting and two degraded resolution settings using the defocusing feature of the display. These measured MTFs are displayed in Figure 3.

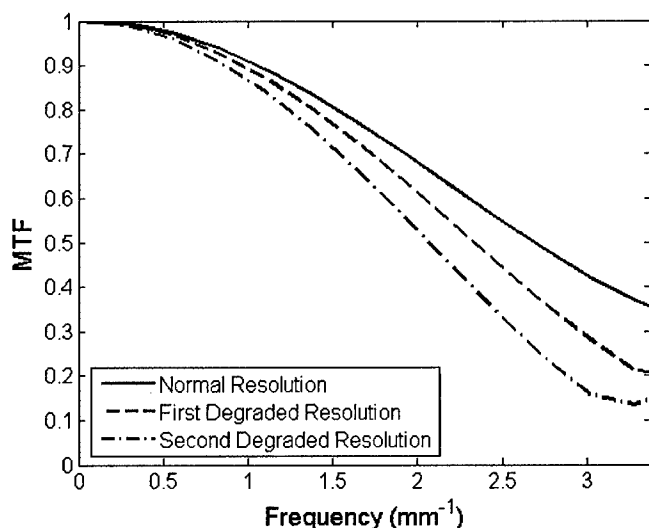


FIG. 3 Measured MTF for a CRT display under three different resolution settings.

2.5 Simulation of Image Display

A Resolution Modification routine, the details of which are disclosed in a previous publication,³⁰ simulated the blur effects of the CRT display. This routine altered the resolution of an input image according to an input MTF to produce a blurred version of the image. To accomplish this, the input mammogram was transformed to the frequency domain through an FFT. The frequency content of the image was then filtered by the display MTF. An inverse FFT transformed this modified frequency spectrum back to the spatial domain. This blurring was performed for each display resolution setting to produce multiple versions of each image.

2.6 Observer Model Experiment

A 5.12 cm x 5.12 cm region of interest (ROI) was extracted from the central breast area for analysis by a visual discrimination model (VDM). The Sarnoff JNDmetrix³³ VDM has been used to simulate the effects of display characteristics and image processing on the conspicuity of mammographic lesions.^{11, 31, 32, 34} For this study, the VDM compared a mammogram containing a lesion to the same mammogram without the lesion and computed a just-noticeable difference (JND) metric for the discriminability of those images by a human observer. The VDM first convolved the input images by an approximation of the point-spread function of the optics of the eye. The model simulated sampling of the image by retinal cones by performing a Gaussian convolution and then point sampling. Next, it computed the local contrast from the raw luminance image. The model applied a Laplacian pyramid to the data in order to isolate five frequency bands from the data. For each frequency band, the data was convolved with eight pairs of spatially oriented filters. The sensitivities and other parameters for these filters were determined by fitting model output to psychophysical data from sine-grating detection and discrimination experiments. The model squared each pair of filter output images and summed them to provide a phase-independent response. Next, the transducer stage derived the energy for each frequency band, normalizing this energy by the square of the appropriate grating contrast detection threshold. A sigmoid function was applied to each frequency band to account for the visual contrast discrimination function. The model incorporated the foveal sensitivity by averaging the outputs from the transducer step using a disk kernel. The final product of the model was a two-dimensional map of JND values, where each pixel indicated the discriminability of the two input images.

3. RESULTS

Figure 4 illustrates the results when the VDM discriminates between mammographic images with simulated benign masses and those without simulated benign masses. The *perfect* resolution refers to images without any display blur, while the other three resolution settings refer to the measured MTFs in Figure 3. As expected, the model was better able to detect masses without any display blur. The difference between the three display blur settings remained much more modest.

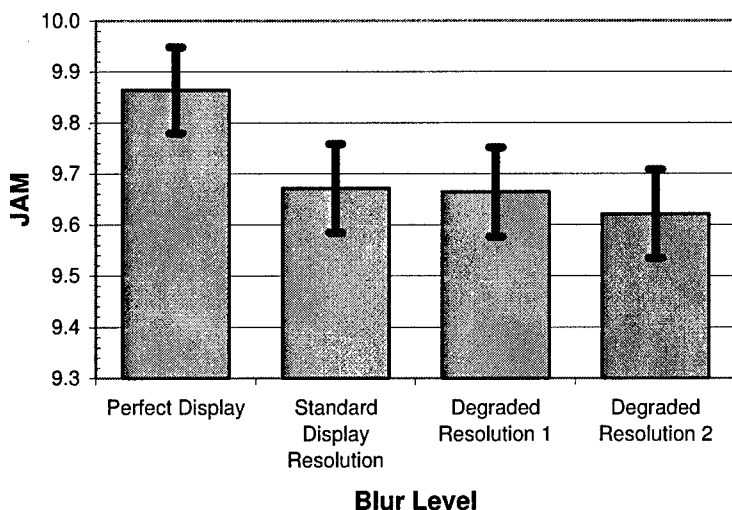


FIG. 4 JND Aggregate Measure (JAM) from the VDM comparing mammographic backgrounds with and without simulated benign masses for four different resolution settings. The benign masses had an average diameter of 3 mm. The error bars represent the 95% Confidence Interval.

Figure 5 illustrates the results when the VDM discriminates between mammographic images with simulated fine linear branching calcifications and those without simulated calcifications. The nomenclature in Figure 5 remains consistent with Figure 4. As expected, the model had a greater ability to detect these calcifications without any display blur. However, as the resolution of the CRT degrades, the detectability of calcifications decreased significantly. Similar model results were obtained for images with pleomorphic calcifications.

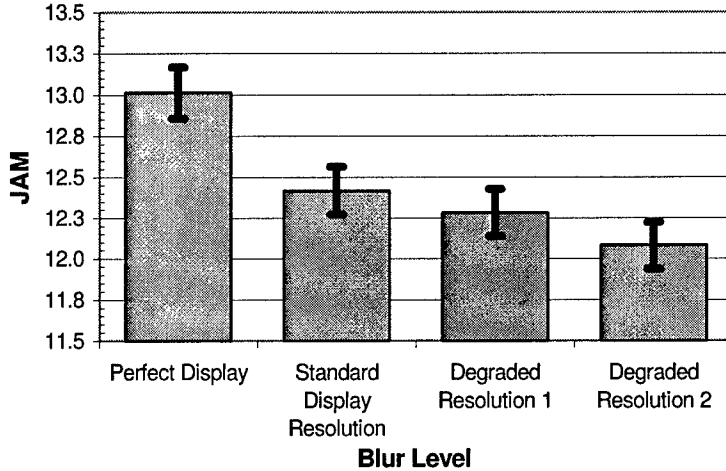


FIG. 5 JND Aggregate Measure (JAM) from the VDM comparing mammographic backgrounds with and without simulated fine linear branching calcifications for four different resolution settings.

4. DISCUSSION AND CONCLUSIONS

This study evaluated the impact of display blur on the detection of mammographic masses and calcifications. As an initial step, this study utilized a visual discrimination model to estimate detection by a human observer. These initial results suggested that detection of masses and calcifications decreased with standard CRT resolution. In addition, the model implies that the detection of calcifications, but not masses, declined as the resolution of the CRT degraded over time. This prediction seems reasonable because the conspicuity of small, fine structures in calcifications are more likely than larger objects, such as masses, to be affected by reductions in display resolution. The next phase of modeling will use VDM output to predict signal detectability within the framework of a channelized model observer. Future work must include human observer performance experiments to verify these estimates.

ACKNOWLEDGEMENTS

The authors thank Jay Baker and Annahita Farshchi for their assistance in this research. In addition, the authors are very grateful to Andrew Karellas and Sankararaman Suryanarayanan of Emory University for the use of their mammographic data set. This work was supported by grants NIH R21-CA95308 and USAMRMC W81XWH-04-1-0323.

References

- ¹ M. J. Flynn and E. Samei, "Experimental comparison of noise and resolution for 2k and 4k storage phosphor radiography systems," *Med Phys* **26**, 1612-1623 (1999).
- ² W. Zhao, I. Blevis, S. Germann, J. A. Rowlands, D. Waechter and Z. S. Huang, "Digital radiology using active matrix readout of amorphous selenium: Construction and evaluation of a prototype real-time detector," *Med Phys* **24**, 1834-1843 (1997).
- ³ E. Samei and M. J. Flynn, "An experimental comparison of detector performance for computed radiography systems," *Med Phys* **29**, 447-459 (2002).
- ⁴ E. Samei and M. J. Flynn, "An experimental comparison of detector performance for direct and indirect digital radiography systems," *Med Phys* **30**, 608-622 (2003).
- ⁵ S. Vedantham, A. Karellas, S. Suryanarayanan, I. Levis, M. Sayag, R. Kleehammer, R. Heidsieck and C. J. D'Orsi, "Mammographic imaging with a small format CCD-based digital cassette: Physical characteristics of a clinical system," *Med Phys* **27**, 1832-1840 (2000).

- 6 O. Tousignant, Y. Demers, L. Laperriere, M. Nishiki, S. Nagai, T. Tomisaki, A. Takahashi and K. Aoki, "Clinical performance of a 14" * 14" real-time amorphous selenium flat-panel detector," Proc. SPIE **5030**, 71-6 (2003).
- 7 B. Lazzari, G. Belli, C. Gori and K. Nykanen, "Physical characteristics of a clinical prototype for full-field digital mammography with an a-Se flat panel detector," Proc. SPIE **5030**, 656-66 (2003).
- 8 S. S. Kang, J. K. Park, D. G. Lee, C. W. Mun, J. H. Kim and S. H. Nam, "X-ray detection properties of polycrystalline Cd/sub 1-x/Zn/sub x/Te detectors for digital radiography," Proc. SPIE **5030**, 853-60 (2003).
- 9 D. C. Hunt, O. Tousignant, Y. Demers, L. Laperriere and J. A. Rowlands, "Imaging performance of an amorphous selenium flat-panel detector for digital fluoroscopy," Proc. SPIE **5030**, 226-34 (2003).
- 10 J. Fan, W. J. Dallas, H. Roehrig, E. A. Krupinski, K. Gandhi and M. K. Sundareshan, "Spatial noise of high-resolution liquid-crystal displays for medical imaging: quantitative analysis, estimation, and compensation," Proc. SPIE **5367**, 433-443 (2004).
- 11 E.A. Krupinski, J. Johnson, H. Roehrig, J. Lubin. "Using a human visual system model to optimize soft-copy mammography display: influence of display phosphor", Acad Radiol **10**, 161-166 (2003).
- 12 A. Badano, R. M. Gagne, R. J. Jennings, S. E. Drilling, B. R. Imhoff and E. Muka, "Noise in flat-panel displays with subpixel structure," Med Phys **31**, 715-723 (2004).
- 13 H. Roehrig, J. Gaskill, J. Fan, A. Poolla and C. Martin, "In-field evaluation of the modulation transfer function of electronic display devices," Proc. SPIE **5367**, 456-463 (2004).
- 14 A. R. Pineda and H. H. Barrett, "What does DQE say about lesion detectability in digital radiography?," Proc. SPIE **4320**, 561-9 (2001).
- 15 H. H. Barrett, "Quality time with the fractious Fourier family [image quality]," Proc. SPIE **4392**, 9-21 (2001).
- 16 H. H. Barrett, "Objective assessment of image quality: effects of quantum noise and object variability," J Opt Soc Am A **7**, 1266-78 (1990).
- 17 J. Fan, W. J. Dallas, H. Roehrig and E. A. Krupinski, "Improving visualization of digital mammograms on the CRT display system," Proc. SPIE **5029**, 746-753 (2003).
- 18 K. D. Compton, "Factors affecting CRT display performance: specifying what works," Proc. SPIE **3976**, 412-23 (2000).
- 19 S. Vedantham, A. Karellas, S. Suryanarayanan, D. Albagli, S. Han, E. J. Tkaczyk, C. E. Landberg, B. Opsahl-Ong, P. R. Granfors, I. Levis, C. J. D'Orsi and R. E. Hendrick, "Full breast digital mammography with an amorphous silicon-based flat panel detector: Physical characteristics of a clinical prototype," Med Phys **27**, 558-567 (2000).
- 20 S. Suryanarayanan, A. Karellas and S. Vedantham, "Physical characteristics of a full-field digital mammography system," Nucl Instrum Methods **533**, 560-570 (2004).
- 21 R. S. Saunders and E. Samei, "Characterization of breast masses for simulation purposes," Proc. SPIE **5372**, 242-250 (2004).
- 22 R. S. Saunders Jr., E. Samei and J. A. Baker, "Simulation of Breast Lesions," 7th International Workshop on Digital Mammography (2004).
- 23 M. Heath, K. Bowyer, D. Kopans, R. Moore and P. Kegelmeyer, "The Digital Database for Screening Mammography," in *Proceedings of the 5th International Workshop on Digital Mammography*, edited by (Medical Physics Publishing, Madison, WI, 2000), Vol. pp
- 24 E. Samei, M. J. Flynn and W. R. Eyler, "Simulation of subtle lung nodules in projection chest radiography," Radiology **202**, 117-24 (1997).
- 25 J. M. Boone, K. K. Lindfors, V. N. Cooper, 3rd and J. A. Seibert, "Scatter/primary in mammography: comprehensive results," Med Phys **27**, 2408-16 (2000).
- 26 M. Stahl, T. Aach and S. Dippel, "Digital radiography enhancement by nonlinear multiscale processing," Med Phys **27**, 56-65 (2000).
- 27 E. Samei, "TG18: A new development in display quality and performance evaluation," Med Phys **29**, 1314-1314 (2002).
- 28 E. Samei and M. J. Flynn, "A method for in-field evaluation of the modulation transfer function of electronic display devices," Proc. SPIE **4319**, 599-607 (2001).
- 29 R. S. Saunders, A. Farshchi and E. Samei, "Resolution and Noise Measurements of Selected Commercial Medical Displays," Med Phys (**In Review, January 2005**),

- 30 R. S. Saunders and E. Samei, "A method for modifying the image quality parameters of digital radiographic
images," *Med Phys* **30**, 3006-3017 (2003).
- 31 W. B. Jackson, M. R. Said, D. A. Jared, J. O. Larimer, J. Gille and J. Lubin, "Evaluation of human vision
models for predicting human observer performance," *Proc. SPIE* **3036**, 64-73 (1997).
- 32 E.A. Krupinski, J. Johnson, H. Roehrig, M. Engstrom, J. Fan, J. Nafziger, J. Lubin, W.J. Dallas. "Using a
human visual system model to optimize soft-copy mammography display: influence of MTF
compensation", *Acad Radiol* **10**, 1030-1035 (2003).
- 33 J. Lubin. "A Visual Discrimination Model for Imaging System Design and Evaluation." In Peli E (Ed.)
Visual Models for Target Detection and Recognition. Singapore: World Scientific Publishers (1995).
- 34 E.A. Krupinski, J. Johnson, H. Roehrig, J. Nafziger, J. Fan, J. Lubin. "Use of a human visual system model
to predict observer performance with CRT vs LCD display of images." *J. Digital Imaging* **17**, 258-263
(2004).

Simulation of Breast Lesions

Robert S Saunders, Jr^{a,b}, Ehsan Samei^{a,b,c}, Jay Baker^b

^a Department of Physics, Duke University

^b Department of Radiology, Duke University Medical Center

^c Department of Biomedical Engineering, Duke University

Abstract

Lesion simulation provides a tool when quantifying the utility of an imaging system in a detection task. For mammography, the important detection tasks are detecting breast masses and calcifications. In this study, we characterized the radiographic appearance of both masses and calcifications from images obtained from the Digital Database of Screening Mammography (DDSM). The characterization results were then used in a routine capable of creating simulated masses and calcifications. To verify the quality of this simulation routine, an observer performance experiment was conducted in which an observer was asked to discriminate between real and simulated lesions. The results were then analyzed using ROC analysis. The preliminary results showed an A_z of 0.59 for benign masses, 0.61 for malignant masses, and 0.58 for malignant calcifications. More observer studies are underway to enhance the statistical power of these results. (This work was supported by a grant from the NIH, R21-CA95308 and USAMRMC W81XWH-04-1-0323.)

1. Introduction

A number of new full-field digital mammography systems with varying attributes have entered the clinical arena. It is important, therefore, to discover which systems are most appropriate for mammographic imaging. As the detection of breast cancer is the key task in mammography, a system should be judged in how well it aids in that task. Simulation techniques significantly facilitate such evaluations for a variety of detectors, breast densities, and lesion types.

One hurdle faced by mammography simulation is the lack of breast lesion models. For masses, previous work has used gaussian profiles, disks, and simulated lung nodule profiles.¹⁻⁴ For calcifications, the most common model has been to utilize masks extracted from real calcifications.^{5,6} This study adopted a different approach. First, we characterized the radiographic appearance of breast masses and calcifications from real mammograms. Then, we created simulated breast masses and calcifications emulating those characteristics. Our mass model was previously validated through a preliminary observer performance experiment.⁷ This paper extends that work to microcalcifications.

2. Lesion Characterization

2.1 Breast Mass Characterization Procedure

Four categories of breast masses were chosen for characterization using the BI-RADS[®] lexicon.⁸ Two types were typically benign, *oval circumscribed* and *oval obscured masses*, and two were typically malignant, *irregular ill-defined* and *irregular spiculated*. Sample mammograms containing these lesions were extracted from the University of South Florida's Digital Database for Screening Mammography (DDSM).⁹ Characterization was performed on a 2.56 cm x 2.56 cm region of interest (ROI) surrounding the mass. All ROIs were converted to optical density values using the characteristic curve of the scanner.

The behavior of the masses was determined through a large-scale analysis and a small-scale analysis. The large-scale behavior was characterized through an elliptical trace, which examined the changes in optical density through concentric elliptical rings. The small-scale behavior was measured through a deviation profile that measured how the border of the lesion varied from an ellipse. These are shown graphically in figure 1.

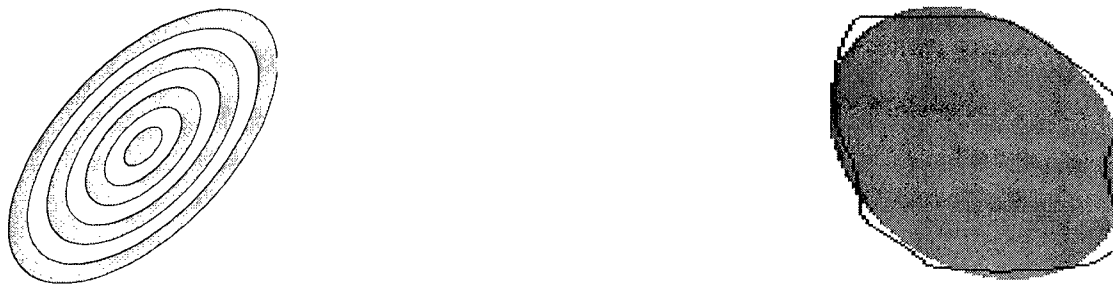


Fig. 1. The elliptical trace, left, characterizes the large-scale behavior of the mass. The small-scale behavior is shown in the border deviation profile, right.

2.2 Breast Mass Characterization Results

Example characterization results for typically benign masses are shown in figure 2. The elliptical trace showed a sharp transition from the mass to the background, which was expected for a circumscribed border. The border deviation profile showed some deviations from the perfect ellipse, but the magnitude was fairly small. This was in contrast to the results for typically malignant masses, an example of which is shown in figure 3. The elliptical trace for these masses showed a very slow transition from the mass to the background. The border deviation profile illustrated strong deviations from the perfect ellipse. This was expected as the borders are ill-defined and the shape was irregular.

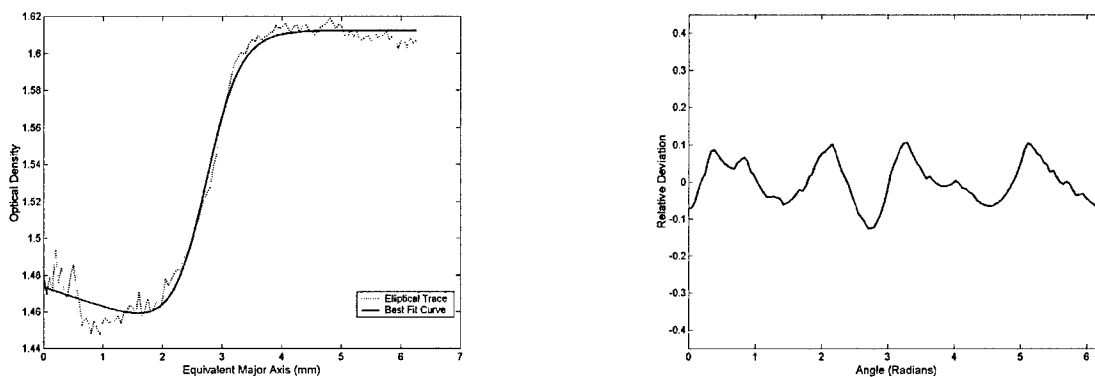


FIG. 2. Example characterization results for benign masses. The elliptical trace, left, shows a strong transition from mass to background while the border deviation profile, right, shows small deviations from the perfect ellipse.

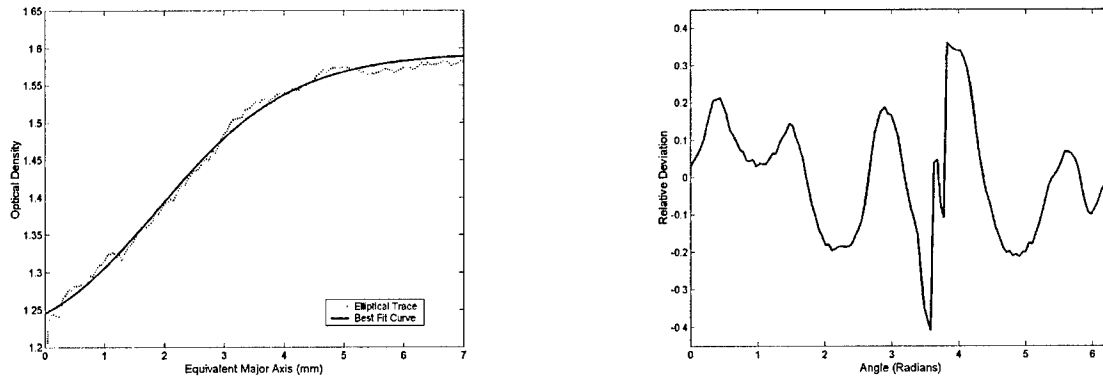


FIG. 3. Example characterization results for malignant masses. The elliptical trace, left, shows a smooth transition to background, and the border deviation profile, right, shows marked deviations from the perfect ellipse.

2.3 Calcification Characterization Procedure

Two categories of calcifications were chosen based on the BI-RADS[®] lexicon.⁸ The two categories were *fine linear branching* and *pleomorphic*, referring to typically malignant lesions. The distribution studied for fine branching calcifications was linear, while the distribution studied for pleomorphic was clustered. Similar to masses, sample mammograms were drawn from the DDSM database.

To characterize the calcifications, a mask of the distribution was drawn. Measurements were then made on this binary mask. Three properties were measured for the individual calcifications: the major axis, minor axis, and the average contrast. Furthermore, the distributions for each calcification type were measured. For pleomorphic calcifications, the major axis and minor axis of the cluster were measured. For fine linear branching calcifications, the lengths of the lines were measured along with the angle between the lines of calcifications.

2.4 Calcification Characterization Results

The results from the calcification characterization are shown in table 1. The individual calcifications results were similar for both pleomorphic and fine linear branching categories.

The distribution results established the mean shape for each distribution.

Table 1. Summary of calcification characterization results

| Calcifications: | Pleomorphic | Fine Linear Branching |
|------------------------|--------------------|------------------------------|
| Major Axis (mm) | 0.47 ± 0.11 | 0.43 ± 0.13 |
| Minor Axis (mm) | 0.29 ± 0.057 | 0.26 ± 0.045 |
| Contrast | 0.22 ± 0.13 | 0.34 ± 0.16 |
| Distribution: | | |
| Major Axis (mm) | 8.0 ± 3.5 | n/a |
| Minor Axis (mm) | 7.1 ± 3.2 | n/a |
| Line Length (mm) | n/a | 6.2 ± 2.3 |
| Angle (degrees) | n/a | 50.8 ± 11.2 |

3. Lesion Simulation

3.1 Mass Simulation

The mass simulation routine began with an array where each pixel was set equal to its equivalent major axis value (given the eccentricity and center location). The border deviation effects were then applied to this array. Finally, the array was transformed to optical density using the elliptical trace profile. This is shown graphically in figure 4. Example masses are shown imbedded in backgrounds in figure 5.

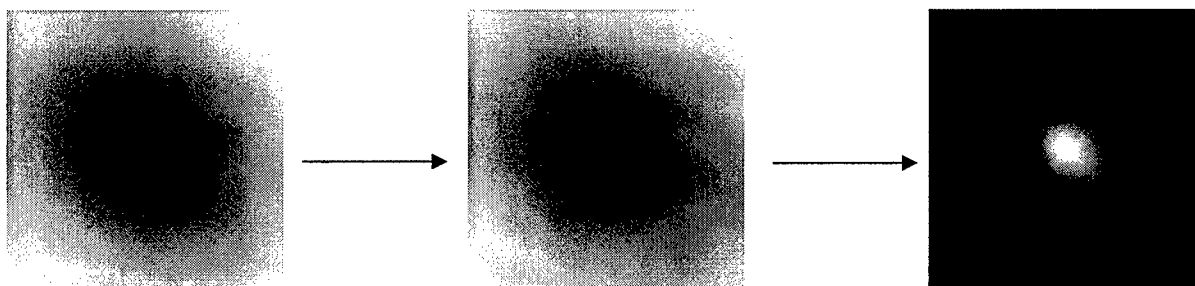


FIG. 4. Graphical overview of mass simulation procedure. The image on left shows an array with pixel values equal to their equivalent major axis value. The border deviations are introduced in the center image. Finally, the image is transformed to optical density through the elliptical trace profile, which results in the final image on the right.

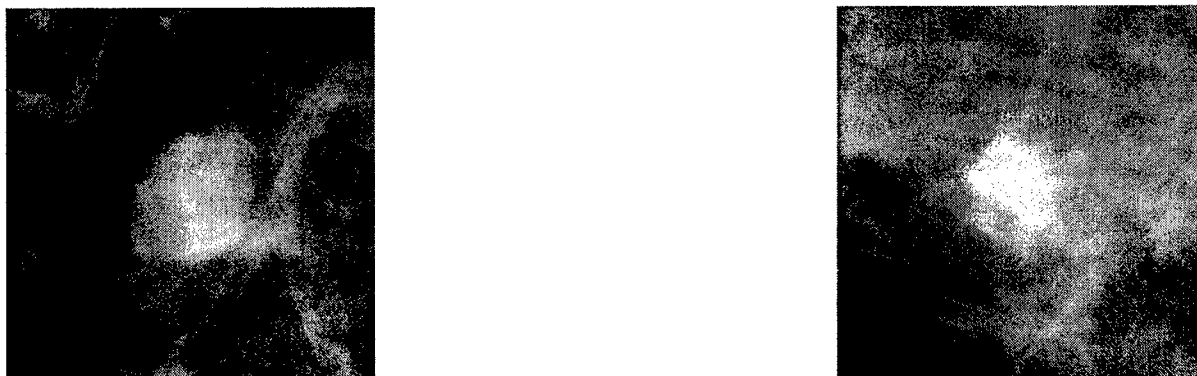


FIG. 5. Example simulated masses. The image on the left is a simulated benign mass, while the image on the right is a simulated malignant mass with an ill-defined border.

3.2 Calcification Simulation

The measured distribution results established a probability distribution for the individual calcification centers. For the pleomorphic category, the centers had a uniform probability density within an ellipse with a given major axis and minor axis length. For the fine, linear branching case, the centers had a uniform probability distribution along lines with a given mean length and relative angle between lines.

Given the desired number of individual calcifications, the simulation program sampled these distributions to determine the location of the centers of the individual calcifications. For each individual calcification, a line was drawn through this center at a random angle. The length of this line was equal to the major axis length of the individual calcifications. A morphological thickening operation was then applied, followed by a morphological eroding. These produced the shapes of the individual calcifications. The calcification distribution was then added to a normal background with a given contrast. Example simulated calcifications were shown in figure 6.

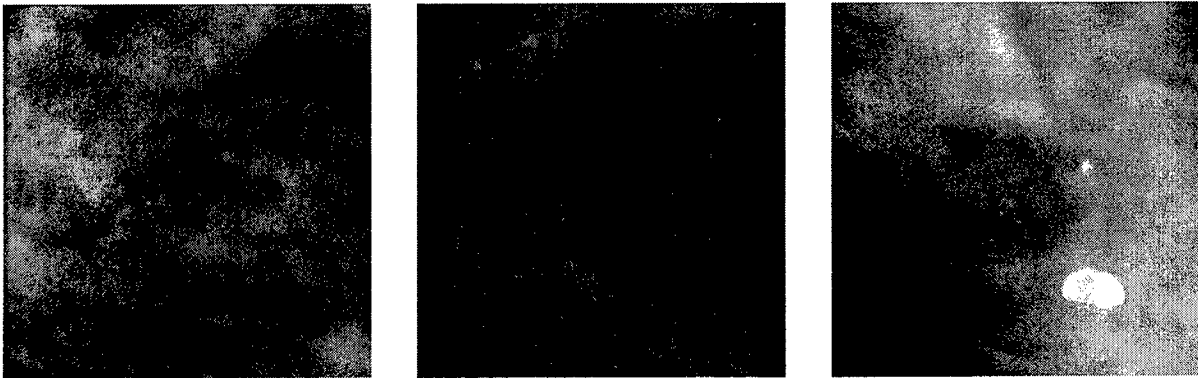


FIG. 6. Example simulated calcifications. The left image shows a simulated pleomorphic distribution, while the center and right image show simulated fine, linear branching calcifications.

4. Observer Performance Experiment

4.1 Observer Protocol

To determine the quality of the simulation routines, an observer performance experiment was conducted. In this study, an experienced mammographer was asked to rate their confidence in whether a lesion was definitely real or definitely simulated. The simulation routine would be effective if a mammographer was unable to distinguish the difference between the simulated and real lesions. As this was a preliminary experiment, only one mammographer was used.

4.2 Observer Results

The histograms for the observer results for masses are shown in figure 7. In general, the distributions for real and simulated masses overlap considerably. The histogram for calcifications is shown in figure 8. Again, the histograms for real and simulated lesions overlap considerably.

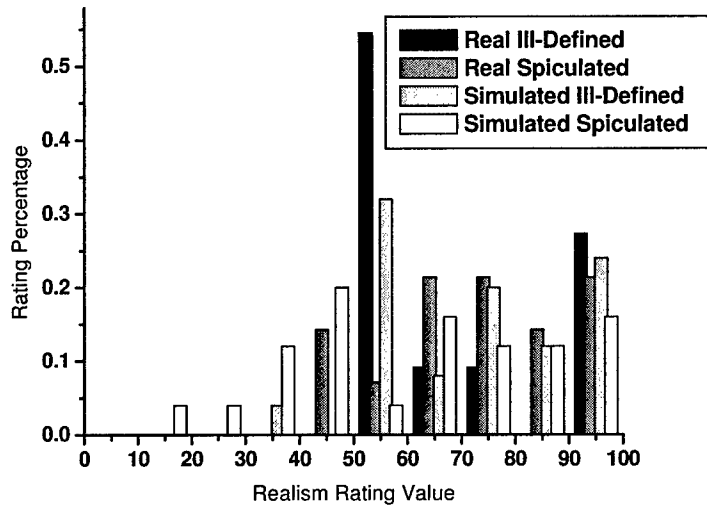
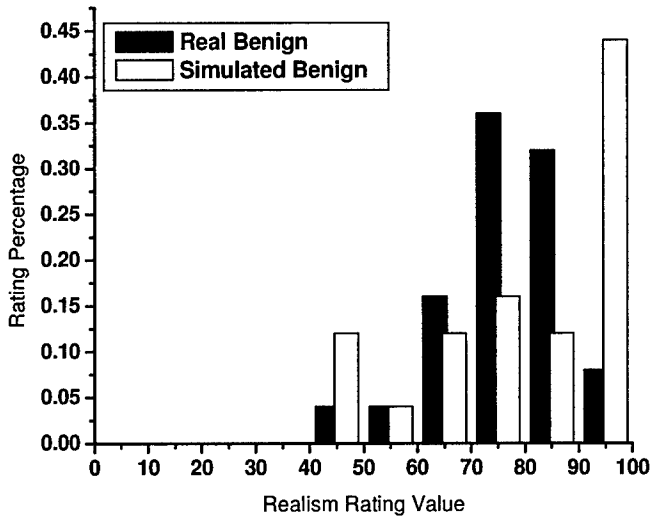


FIG. 7. Histograms of the rating frequency versus rating value for real and simulated masses. The results for typically benign masses are shown on the top while the typically malignant mass results are shown on the bottom. The typically malignant masses are further separated by border type for real and simulated masses.

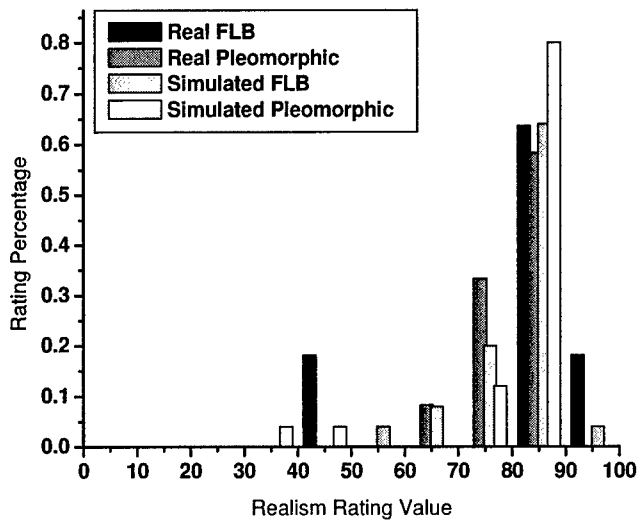


FIG. 8. Histogram of the rating frequency versus rating value for calcifications.

To quantify the degree of overlap, a Receiver Operating Characteristic Analysis was performed.¹⁰ In this case, an A_z of 0.5 indicates that an observer was near chance in discriminating between real and simulated lesions. This analysis is summarized in table 2.

Table 2. Summary of ROC Analysis for discrimination between real and simulated lesions.

| | A_z | σ |
|--------------------------|-------|----------|
| Benign Masses | 0.59 | 0.08 |
| Malignant Masses | 0.61 | 0.07 |
| Malignant Calcifications | 0.58 | 0.07 |

5. Conclusions

The characterization procedure undertaken in this study introduces a new way to describe breast lesions. The data from this characterization was then used in a new simulation routine that is capable of simulating breast masses and calcifications. Results from a preliminary observer performance experiment on these simulations indicate that our simulation routine produces high quality simulations of breast masses and calcifications. Further work is needed to validate the results of this preliminary observer performance experiment.

Acknowledgements

Thanks to Joseph Lo for his assistance in this project. This work was partially supported by a grant from the NIH, R21-CA95308, and from USAMRMC, W81XWH-04-1-0323.

References

- 1 D. P. Chakraborty and H. L. Kundel, "Anomalous nodule visibility effects in mammographic images," Proc. SPIE **4324**, 68-76 (2001).
- 2 C. K. Abbey, M. P. Eckstein, S. S. Shimozaki, A. H. Baydush, D. M. Catarious and C. E. Floyd, "Human-observer templates for detection of a simulated lesion in mammographic images," Proc. SPIE **4686**, 25-36 (2002).
- 3 W. Huda, G. Qu, Z. Jing, B. G. Steinbach and J. C. Honeyman, "How does observer training affect imaging performance in digital mammography?," Proc. SPIE **3981**, 259-266 (2000).
- 4 A. E. Burgess, "Evaluation of detection model performance in power-law noise," Proc. SPIE **4324**, 123-32 (2001).
- 5 F. Lefebvre, H. Benali, R. Gilles and R. Di Paola, "A simulation model of clustered breast microcalcifications," Med Phys **21**, 1865-74 (1994).
- 6 M. Kallergi, M. A. Gavrielides, L. He, C. G. Berman, J. J. Kim and R. A. Clark, "Simulation model of mammographic calcifications based on the American College of Radiology Breast Imaging Reporting and Data System, or BIRADS," Acad Radiol **5**, 670-9 (1998).
- 7 R. S. Saunders and E. Samei, "Characterization of breast masses for simulation purposes," Proc. SPIE **5372**, 242-250 (2004).
- 8 C. D'Orsi, et al, Illustrated Breast Imaging Reporting and Data System (BI-RADS) (American College of Radiology, Reston, VA, 1998).
- 9 M. Heath, K. Bowyer, D. Kopans, R. Moore and P. Kegelmeyer, "The Digital Database for Screening Mammography," in *Proceedings of the 5th International Workshop on Digital Mammography*, edited by (Medical Physics Publishing, Madison, WI, 2000).
- 10 C. E. Metz, B. A. Herman and J. H. Shen, "Maximum likelihood estimation of receiver operating characteristic (ROC) curves from continuously-distributed data," Stat Med **17**, 1033-1053 (1998).

Physical Characterization of a Selenium-based Full Field Digital Mammography Detector

Robert S. Saunders, Jr.^{a,b}, Ehsan Samei^{a,b,c}, Joseph Lo^{b,c}, Jonathan Jesneck^{b,c}

^aDepartment of Physics, Duke University

^bDuke Advanced Imaging Labs, Department of Radiology, Duke University Medical Center

^cDepartment of Biomedical Engineering, Duke University

Abstract

Digital mammography has the potential to improve image quality for mammographic imaging. This study evaluated a selenium-based direct full-field digital mammographic imager (70 μm pixels) using a molybdenum anode operated at 28 kVp with inherent filtration of 30 μm molybdenum and an additional 2 mm of aluminum filtration. To capture the detector resolution, we measured the presampled modulation transfer function (MTF) using an edge method. The noise, summarized through the Normalized Noise Power Spectrum (NNPS), was measured by two-dimensional Fourier analysis of uniformly exposed radiographs. The detective quantum efficiency (DQE) was then computed from the measured MTF, NNPS, and ideal signal-to-noise ratio. For the Left-Right axis, the MTF reached the value of 0.2 and 0.1 at 12.7 mm^{-1} and 14.8 mm^{-1} , respectively. The DQE attained a maximum value of 53% at 1.45 mm^{-1} for the Left-Right axis. However, the DQE showed a strong dependence on exposure and frequency. The results indicated that this detector has high resolution, but it may be valuable to remove structured noise through improved calibration before clinical implementation. (The full data for this study are published as R.S. Saunders, Jr, E. Samei, J.L. Jesneck, and J.Y. Lo, "Physical characterization of a prototype selenium-based full field digital mammography detector," *Med. Phys.* 32(2) (2005).

1. Introduction

The purpose of this work was to evaluate the physical characteristics of a selenium full-field digital mammography (FFDM) detector. Three different metrics of system performance were evaluated: the Modulation Transfer Function (MTF), Normalized Noise Power Spectrum (NNPS), and Detective Quantum Efficiency (DQE). As previous research has shown that selenium detectors can exhibit image lag and ghosting,¹ this research also examined the lag performance of the detector.

2. Methods and Materials

2.1 Detector Description

The detector investigated in this study was a selenium-based flat-panel detector (Siemens Medical Systems, Erlangen, Germany). The detector was based on a 250 μm selenium photoconductive layer coupled to a storage capacitor and amorphous selenium switching transistor.² The active detector area was 23.296 cm x 28.672 cm consisting of 3328 x 4096 square pixels with a 70 μm pixel pitch. Prior to evaluation, the antiscatter grid supplied with the system was removed and gain and dead pixel corrections were performed according to manufacturer specifications. For most measurements, the standard detector cover was kept in place and the compression paddle was removed. For the MTF measurements, the detector cover was removed so that the edge device could be placed in contact with the detector.

2.2 Image Acquisition

The selenium detector was coupled to a high frequency multiphase x-ray generator (Mammomat Novation) for which the high-voltage accuracy was certified to be within $\pm 5\%$. All images were

acquired with a large focal spot of 0.3 mm, nominal. We used the RQA-M2 technique,³ which employed a molybdenum anode operated at 28 kVp, 30 μm molybdenum inherent filtration, and 2 mm aluminum added filtration. The image data were acquired in a raw format without any image post-processing applied. After acquisition, the images were transferred to a research computer as 14-bit, raw data for analysis.

For all image acquisitions, the exposure to the detector was measured free in air using a calibrated ionization chamber (1515 x-ray monitor with 10X5-6M dedicated mammography ionization chamber, Radcal Corporation, Monrovia, CA). The chamber was placed 17 cm above the detector to minimize contributions from backscatter. The exposure incident on the detector at 65 cm source to image distance (SID) was estimated from the measured exposure using the inverse-square law.

2.3 Linearity

The linearity of the detector was determined by exposing the detector to a wide range of uniform x-ray exposures for each of the radiographic techniques described above. The average pixel values were computed from a 14.3 x 14.3 cm region located near the chest wall section of the detector. From this, the relationships between mean pixel value and exposure were ascertained.

2.4 Modulation Transfer Function

The presampled MTF was measured using an edge method similar to that reported elsewhere.⁴⁻⁹ A sharp edge test device, consisting of a polished 0.1 mm platinum-iridium edge, was placed in contact with the detector at 1 cm from the chest wall edge of the detector. The device was oriented with a 5–10 degree angle with respect to the pixel array. An image of the edge device

was then acquired using an exposure of 16.2 $\mu\text{C}/\text{kg}$ (62.6 mR). The presampled modulation transfer function (MTF) was then computed from the edge image using a method described in a previous publication.¹⁰ The MTF was computed along two orthogonal directions—the Chest Wall-Nipple (CN) axis and the Left-Right (LR), as shown in Figure 1.

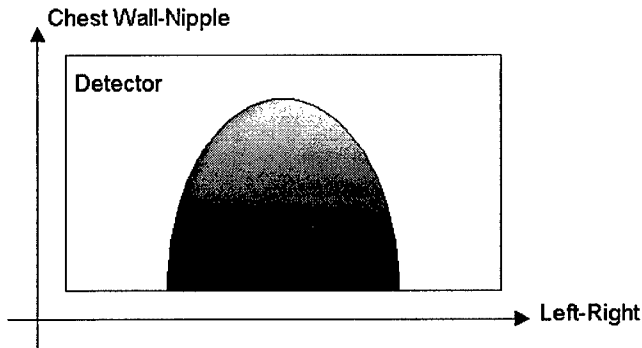


FIG. 1. Coordinate system for measurements

2.5 Normalized Noise Power Spectrum

To characterize the system noise, flat-field images were acquired by exposing the detector to a uniform x-ray beam. The exposure was simultaneously measured with the ionization chamber reported above. The Normalized Noise Power Spectrum was then computed from the flat-field images using previously published methods.^{9, 10}

2.6 Detective Quantum Efficiency

The Detective Quantum Efficiency (DQE) was computed using the following equation:

$$DQE(u) = \frac{MTF^2(u)}{q_{Ideal}^2 \cdot E \cdot NNPS(u)} \quad (1)$$

where $MTF(u)$ represented the presampled modulation transfer function measured above, q_{Ideal} corresponded to the signal to noise (SNR) ratio per unit exposure for an ideal energy-integrating detector, E was the exposure value at the detector face at which the Normalized Noise Power Spectrum, $NNPS(u)$, was measured.^{11, 12} The q_{Ideal} was computed with an x-ray simulation program (xSpect, Henry Ford Health System) that utilized a semiempirical model to simulate the x-ray spectra¹³ and attenuation effects.⁵

2.7 Image Lag Measurement

The magnitude of multiplicative lag was characterized using the procedure described in IEC 62220-1.¹⁴ First, an image was acquired of a uniform radiation field. The second image was then acquired of an edge device. After a specified delay time Δt , a third image was acquired of a uniform radiation field. The image data were then examined for two regions within the images. The first ROI, ROI_1 , was placed in an area of the images that did not contain the edge device in image 2. The second ROI, ROI_2 , was placed in an area that was inside the region covered by the edge device in image 2.

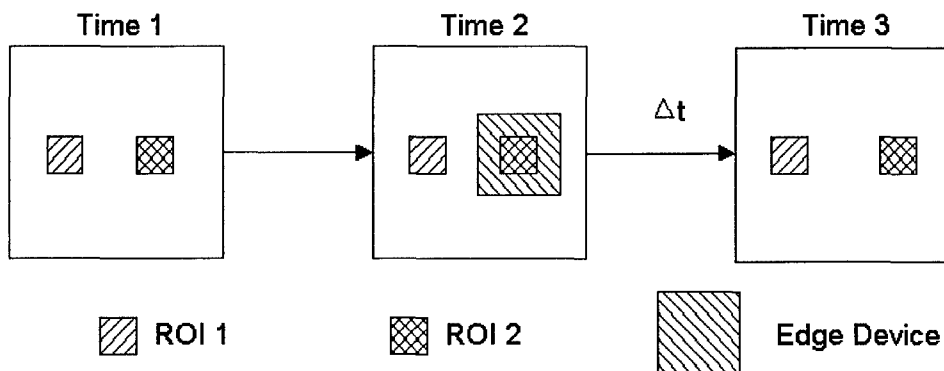


FIG. 2. Description of the lag measurement procedure.

The detector was judged to have acceptable lag effects for time delay Δt if it passed the following criterion¹⁴

$$\left| \frac{(\text{Image1}_{\text{ROI1}} - \text{Image1}_{\text{ROI2}}) - (\text{Image3}_{\text{ROI1}} - \text{Image3}_{\text{ROI2}})}{\frac{\text{Image1}_{\text{ROI2}} + \text{Image3}_{\text{ROI2}}}{2}} \right| \leq 0.005 \quad (2)$$

3. Results

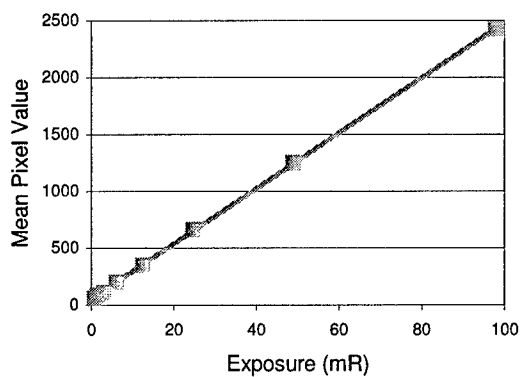


FIG. 3. Plot of mean pixel value versus exposure. The system showed a very linear response with $r^2 > 0.999$.

The large area transfer characteristics of the detector are shown in figure 3. The detector maintains its linearity over two orders of magnitude in exposure. The MTF is shown in figure 4 for the CN and LR axis. The MTF along these axes diverge at higher spatial frequencies. The MTF curves are summarized in Table I for each axis.

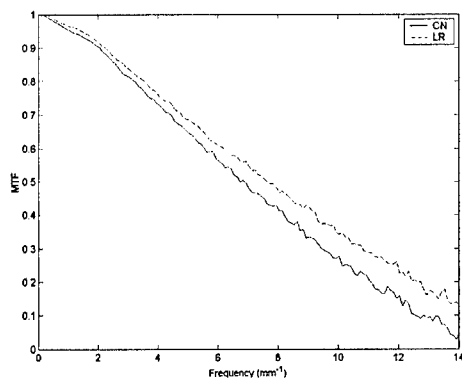


FIG. 4. Plot of detector MTF for CN and LR axes

| | RQA-M2 (CN Axis) | RQA-M2 (LR Axis) |
|----------------------|-----------------------------|-----------------------------|
| 0.2 MTF | 11.1 mm ⁻¹ | 12.7 mm ⁻¹ |
| 0.1 MTF | 12.8 mm ⁻¹ | 14.8 mm ⁻¹ |
| 0.5 mm ⁻¹ | 0.983 | 0.991 |
| 2.5 mm ⁻¹ | 0.858 | 0.877 |
| 5.0 mm ⁻¹ | 0.65 | 0.689 |

Table I. Summary of the detector's MTF properties

The radial traces of the NNPS multiplied by exposure are shown in figure 5 for each radiographic technique. The product of NNPS and exposure should remain constant for strictly quantum noise-limited detectors. However, the system exhibited exposure dependencies. For lower exposures, the magnitude of this metric first decreased and then increased with increasing exposure.

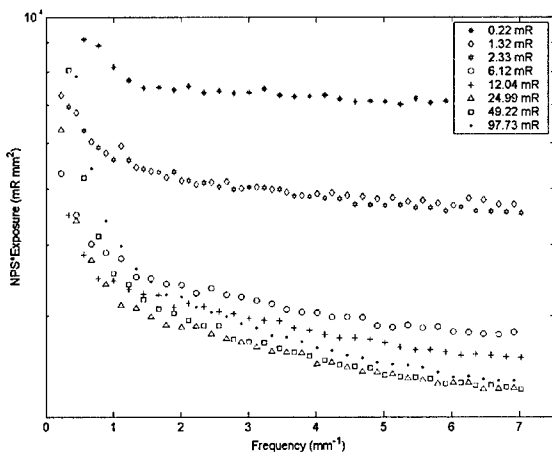


FIG. 5. Radial trace of NNPS for various exposure levels

Figure 6 shows the measured DQE. The DQE curves showed a decline at low frequency, which was expected from the strong low-frequency component of the NNPS. As well, the DQE increased with exposure for lower exposure values, reached a peak value, and then decreased for

higher exposures. This was also expected from the behavior of the NNPS with exposure. The DQE is summarized in table II.

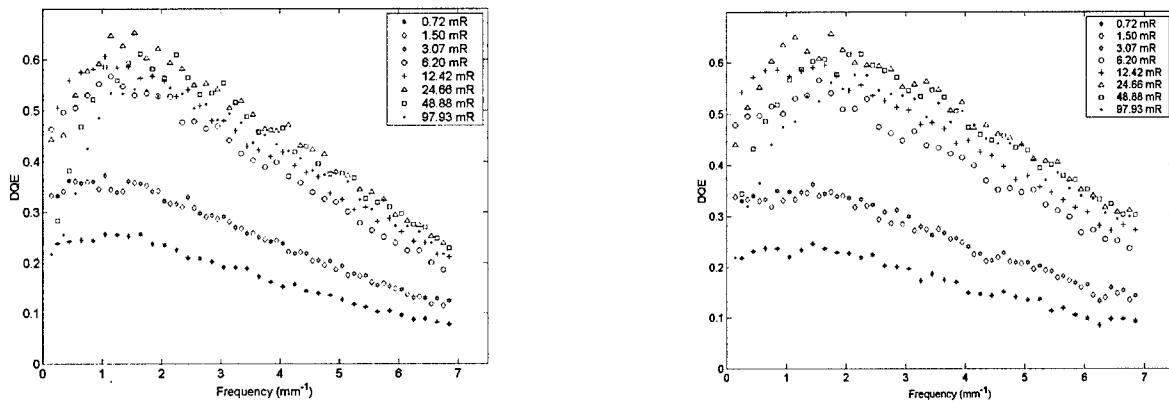


Fig. 6 Plots of the DQE at various exposures along CN axis, left, and LR axis, right.

Table II. Detector DQE properties for CN and LR axes at $1.6 \mu\text{C/kg}$ (6.2 mR)

| | CN Axis | LR Axis |
|------------------------|------------------------|------------------------|
| 0.15 mm^{-1} | 46% | 47% |
| 2.5 mm^{-1} | 49% | 50% |
| 5.0 mm^{-1} | 31% | 34% |
| Peak | 55% | 53% |
| | 1.25 mm^{-1} | 1.45 mm^{-1} |

The results from lag measurements are summarized in table III. The images were acquired in the order indicated in table 3, with shorter delay time tests preceding longer delay time tests. In general, the image lag for the detector passed the test established by the IEC (Eq 2). However, an interesting phenomenon occurred for the $75 \mu\text{Gy}$ exposure with 5 minute delay. A $200 \mu\text{Gy}$ exposure was acquired 10 minutes before this exposure. It appeared that this high exposure still affected the detector after 10 minutes, as a $75 \mu\text{Gy}$ exposure should not have caused a larger lag contribution after a 5 minute decay time than it would after a 3 minute decay time.

Table III. Summary of Multiplicative Lag Measurements

| Exposure (μGy) | Decay Time (min) | Metric | Acceptable? |
|---|-------------------------|---------------|--------------------|
| 75 | 3 | 0.002 | Yes |
| 150 | 3 | 0.0048 | Yes |
| 200 | 3 | 0.0044 | Yes |
| | Ten Minute Wait | | |
| 75 | 5 | 0.047 | No |
| 150 | 5 | 0.013 | No |
| 200 | 5 | 0.0022 | Yes |

4. Discussion

This prototype detector has excellent resolution properties, as shown by its MTF. There appeared to be an asymmetry in the MTF, as it diverged for the CN and LR axes. As the edge device was placed directly on the detector surface, it appeared unlikely that the focal spot caused such asymmetries. Future work is needed to understand the cause of this asymmetry. The prototype showed structured noise contributions, which led to a strong low-frequency contribution to the NNPS. This structured noise also affected the DQE, in that the DQE curves had a peak and then decreased for lower frequencies. Finally, image lag appeared to be within the parameters established by IEC 62220-1,¹⁴ but high exposures led to unusual behavior in signal retention, even after a long decay. This prototype showed excellent promise and it is expected that future work will correct the observed structured noise and lag phenomena with a more robust calibration technique.

Acknowledgements

The authors would like to thank Jim Dobbins and Carey Floyd for several helpful conversations and Thomas Mertelmeier of Siemens Medical Systems for his assistance with this project. This

work was partially supported by a grant from Siemens Medical Systems and USAMRMC

W81XWH-04-1-0323.

References

- 1 W. Zhao, G. DeCrescenzo and J. A. Rowlands, "Investigation of lag and ghosting in amorphous selenium flat-panel X-ray detectors," *Proc. SPIE* **4682**, 9-20 (2002).
- 2 J. G. Yorker, L. S. Jeromin, D. L. Y. Lee, E. F. Palecki, K. P. Golden and Z. Jing, "Characterization of a full-field digital mammography detector based on direct X-ray conversion in selenium," *Proc. SPIE* **4682**, 21-9 (2002).
- 3 International Electrotechnical Commission, Medical diagnostic X-ray equipment - Radiation conditions for use in the determination of characteristics (IEC-61267, Geneva, Switzerland, 2003).
- 4 E. Samei, M. J. Flynn, H. G. Chotas and J. T. Dobbins, III, "DQE of direct and indirect digital radiographic systems," *Proc. SPIE* **4320**, 189-97 (2001).
- 5 E. Samei and M. J. Flynn, "An experimental comparison of detector performance for computed radiography systems," *Med Phys* **29**, 447-459 (2002).
- 6 E. Samei and M. J. Flynn, "An experimental comparison of detector performance for direct and indirect digital radiography systems," *Med Phys* **30**, 608-622 (2003).
- 7 E. Samei, "Image quality in two phosphor-based flat panel digital radiographic detectors," *Med Phys* **30**, 1747-57 (2003).
- 8 E. Samei, M. J. Flynn and D. A. Reimann, "A method for measuring the presampled MTF of digital radiographic systems using an edge test device," *Med Phys* **25**, 102-113 (1998).
- 9 M. J. Flynn and E. Samei, "Experimental comparison of noise and resolution for 2k and 4k storage phosphor radiography systems," *Med Phys* **26**, 1612-1623 (1999).
- 10 R. S. Saunders and E. Samei, "A method for modifying the image quality parameters of digital radiographic images," *Med Phys* **30**, 3006-3017 (2003).
- 11 J. C. Dainty and R. Shaw, *Image science : principles, analysis and evaluation of photographic-type imaging processes* (Academic Press, London ; New York, 1974).
- 12 J. Dobbins, "Image Quality Metrics for Digital Systems," in *Handbook of Medical Imaging*, edited by H. K. J. Beutel and R. V. Metter (SPIE, Washington, DC, 2000), Vol. 1, pp 163-222.
- 13 E. Storm, "Calculated bremsstrahlung spectra from thick tungsten targets," *Phys. Rev. A* **5**, 2328-38 (1972).
- 14 International Electrotechnical Commission, Medical electrical equipment - Characteristics of digital X-ray imaging devices - Part 1: Determination of the detective quantum efficiency (IEC 62220-1, Geneva, Switzerland, 2003).